







Initiation and Early Kinematic Evolution of Solar Eruptions

X. Cheng^{1,2,3} , J. Zhang⁴, B. Kliem⁵ , T. Török⁶ , C. Xing^{1,3}, Z. J. Zhou⁷, B. Inhester², and M. D. Ding^{1,3} 

¹School of Astronomy and Space Science, Nanjing University, Nanjing 210023, People's Republic of China; xincheng@nju.edu.cn

²Max Planck Institute for Solar System Research, Göttingen, D-37077, Germany

³Key Laboratory of Modern Astronomy and Astrophysics (Nanjing University), Ministry of Education, Nanjing 210093, People's Republic of China

⁴Department of Physics and Astronomy, George Mason University, Fairfax, VA 22030, USA

⁵Institute of Physics and Astronomy, University of Potsdam, D-14476 Potsdam, Germany

⁶Predictive Science Inc., 9990 Mesa Rim Road, Suite 170, San Diego, CA 92121, USA

⁷School of Atmospheric Sciences, Sun Yat-sen University, Zhuhai, Guangdong, 519000, People's Republic of China

Received 2019 October 7; revised 2020 March 24; accepted 2020 April 7; published 2020 May 8

Abstract

We investigate the initiation and early evolution of 12 solar eruptions, including six active-region hot channel and six quiescent filament eruptions, which were well observed by the Solar Dynamics Observatory, as well as by the Solar Terrestrial Relations Observatory for the latter. The sample includes one failed eruption and 11 coronal mass ejections, with velocities ranging from 493 to 2140 km s⁻¹. A detailed analysis of the eruption kinematics yields the following main results. (1) The early evolution of all events consists of a slow-rise phase followed by a main-acceleration phase, the height–time profiles of which differ markedly and can be best fit, respectively, by a linear and an exponential function. This indicates that different physical processes dominate in these phases, which is at variance with models that involve a single process. (2) The kinematic evolution of the eruptions tends to be synchronized with the flare light curve in both phases. The synchronization is often but not always close. A delayed onset of the impulsive flare phase is found in the majority of the filament eruptions (five out of six). This delay and its trend to be larger for slower eruptions favor ideal MHD instability models. (3) The average decay index at the onset heights of the main acceleration is close to the threshold of the torus instability for both groups of events (although, it is based on a tentative coronal field model for the hot channels), suggesting that this instability initiates and possibly drives the main acceleration.

Unified Astronomy Thesaurus concepts: [Solar coronal mass ejections \(310\)](#); [Stellar coronal mass ejections \(1881\)](#); [Solar storm \(1526\)](#)

Supporting material: animation

1. Introduction

Coronal mass ejections (CMEs) are the largest explosive phenomena in the solar system. Occurring in the solar atmosphere, they can eject a large quantity of plasma and magnetic flux into the interplanetary space. When the magnetized plasma arrives at the Earth, it will interact with the magnetosphere, potentially producing severe space weather effects, thus affecting the safety of human high-tech activities, especially in outer space (Gosling 1993; Webb et al. 1994).

White-light coronagraph observations revealed that CMEs often have a three-part structure: a bright front followed by a bright core embedded in a dark cavity (Illing & Hundhausen 1983). The bright front originates from plasma pile-up at the front of the expanding CME (e.g., Vourlidas et al. 2003; Cheng et al. 2014a). The cavity, or its central part, is usually interpreted to be a coherent helical flux rope (e.g., Dere et al. 1999; Gibson & Fan 2006; Riley et al. 2008; Song et al. 2017). The bright core represents dense plasma usually attributed to an erupting filament/prominence, which is suspended in magnetic dips of a flux rope or in a sheared arcade prior to the eruption (e.g., Guo et al. 2010; Inoue et al. 2013; Jiang et al. 2014; Su et al. 2015; Yan et al. 2015), but it can also consist of swept-up loops (Veronig et al. 2018). Sometimes, a fourth component, a shock,

appears at the front and flanks of the CME, if its expansion velocity exceeds the local Alfvén speed (Vourlidas et al. 2003; Kwon et al. 2014).

The kinematic evolution of CMEs is usually comprised of three phases: a slow-rise phase of approximately uniform velocity, an impulsive main-acceleration phase, and a propagation phase with only slowly varying velocity (Zhang et al. 2001, 2004). The slow-rise and main-acceleration phases are often also displayed by an associated filament/prominence eruption (e.g., Sterling et al. 2007, 2011).

To understand the initiation and early evolution of CMEs, the relationship between their kinematic evolution and the light curve of their associated flares has been studied extensively. The three CME evolution phases were found to correspond to, respectively, the pre-flare phase, rise phase, and decay phase of the associated flare in soft X-rays (SXR; Neupert et al. 2001; Zhang et al. 2001, 2004; Cheng et al. 2010; Bein et al. 2012). This is further supported by a statistical study of a sample of 22 CMEs performed by Maričić et al. (2007). However, those authors pointed out that the onset of the flare rise phase was delayed with respect to the onset of the CME main-acceleration phase in some of their events. In addition, Qiu et al. (2004) and Temmer et al. (2008, 2010) uncovered that the acceleration of CMEs and the hard X-ray flux of the associated flares are often synchronized as well. These results strongly suggest that CMEs and flares are two distinct manifestations of the same process (or processes), which is a violent disruption of the coronal magnetic field (e.g., Forbes 2000).

The kinematic evolution of a CME low in the corona can be obtained by following the eruption of features of the pre-eruptive configuration. The most common tracers of pre-eruptive configurations are filaments/prominences, which are cool and dense plasma embedded in the hot and tenuous corona (Mackay et al. 2010). Statistically, over 70% of CMEs are associated with erupting filaments/prominences (e.g., Munro et al. 1979; Webb & Hundhausen 1987; Gopalswamy et al. 2003). In addition to the association with erupting filaments/prominences, Cheng et al. (2011) and Zhang et al. (2012) discovered that the pre-eruptive configuration can also manifest as a hot plasma channel (or hot blob when viewed along its axis) in the Atmospheric Imaging Assembly (AIA; Lemen et al. 2012) 131 and 94 Å passbands. Interestingly, hot channels keep a coherent structure throughout the eruption (Zhang et al. 2012; Cheng et al. 2013b; Patsourakos et al. 2013; Nindos et al. 2015). This ensures that their heights (e.g., their distance from the solar surface) can be measured continuously and reliably in the whole AIA field of view.

When studying CME kinematics, the CME bright front is usually used to infer the CME height. This is, however, inappropriate when studying the early evolution of CMEs. Through analyzing a limb CME event, Patsourakos et al. (2010a) found that the CME originated from the fast expansion of a plasma bubble (also see Patsourakos et al. 2010b; Wan et al. 2016). They showed that the kinematic evolution of the CME actually included two components, one being associated with the lifting of the CME centroid (the geometric center of the bubble), and the other with the expansion of the CME bubble. Furthermore, Cheng et al. (2013b) investigated the formation of two CMEs from erupting hot channels and found that the expansion of the channels coincided in time with the expansion of the CME bubbles. Moreover, they found that the hot channel rose faster than the front of the CME bubble during the main-acceleration phase (also see Veronig et al. 2018). These results suggest that hot channels behave as a central engine that drives the formation and acceleration of CMEs during their early stage, and they are therefore a better tracer of the CME kinematics in this phase.

Several mechanisms have been suggested to explain the initiation of CMEs (e.g., Green et al. 2018). One category of mechanisms includes tether-cutting reconnection (Moore et al. 2001) and breakout reconnection (Antiochos et al. 1999; Karpen et al. 2012). The former takes place in the center of sigmoids low in the corona and transforms sheared arcades into a flux rope, which then lifts off, driven by the rope’s magnetic pressure, as a consequence of reduced line tying (e.g., Liu et al. 2010; Chen et al. 2014). The breakout mechanism resorts to reconnection at a high-lying X-line (or null point) located between central sheared flux and overlying flux connecting the outer polarities in a quadrupolar magnetic configuration. By removing the constraint of the overlying flux, the downward tension is reduced, allowing the central flux to escape (e.g., Gary & Moore 2004; Shen et al. 2012).

A second category invokes ideal MHD instabilities such as the torus instability (Kliem & Török 2006; Olmedo & Zhang 2010) and the helical kink instability (Sakurai 1976; Fan & Gibson 2003; Kliem et al. 2004). The torus instability refers to the expansion instability of a toroidal current channel (flux rope), which commences if the decay index of the background field exceeds the critical value of ~ 1.5 (Kliem & Török 2006). Considering a more realistic flux rope structure

that resembles a line-tied partial torus, Olmedo & Zhang (2010) pointed out that the critical value depends on the ratio of the arc length of the partial torus and the circumference of a circular torus with equal radius. Démoulin & Aulanier (2010) and Kliem et al. (2014) demonstrated that the torus instability is equivalent to a catastrophic loss of equilibrium in the MHD framework (Forbes & Isenberg 1991; Lin & van Ballegooyen 2002). In addition to the torus instability, the helical kink instability can also initiate the eruption of a flux rope, if its twist number exceeds a certain threshold (Fan & Gibson 2004; Török et al. 2004). The latter varies for different flux rope configurations (Baty 2001). Once the helical kink instability takes place, the flux rope axis will writhe and present a distinct inverse- γ or Ω morphology (e.g., Ji et al. 2003; Williams et al. 2005; Török et al. 2010; Hassanin & Kliem 2016; Song et al. 2018). However, the observations indicate that this instability is unlikely a universal onset mechanism for solar eruptions, because a critical twist appears to be reached only in a minority of their source regions. Moreover, this instability is not generally suited as a mechanism for the main CME acceleration over a large height range, because it tends to saturate quickly.

The height–time profile of CMEs, $h(t)$, in the early phase of an eruption, and its association with the SXR flare light curve, or flux temporal profile, $F_{\text{SXR}}(t)$, can help to differentiate between initiation models in three ways, which will be addressed in the present paper. First, the existence of a break between the slow-rise and main-acceleration phases argues against the suggestion that a single process (e.g., “runaway reconnection”) is the primary driver of the whole eruption. Second, any temporal offset between $h(t)$ and $F_{\text{SXR}}(t)$ favors ideal MHD models if $h(t)$ is preceding, while it favors reconnection models if $F_{\text{SXR}}(t)$ is preceding and the relevant flare onset is not masked by precursor activity. Third, any correlation between the onset of eruptions, either of the slow-rise or main-acceleration phases, and the threshold of the torus or helical kink instability favors the ideal MHD model, because the threshold should not play any role in the reconnection models.

There have been many investigations of CME height–time curves. Most have found an amplifying acceleration in the main-acceleration phase in basic agreement with all models, i.e., with instability, both ideal and resistive, and with the idea of runaway reconnection. Acceleration profiles close to an exponential (Vršnak 2001; Gallagher et al. 2003; Williams et al. 2005) or close to a power law (Kahler et al. 1988; Vršnak 2001; Alexander et al. 2002; Schrijver et al. 2008) were typically found. Schrijver et al. (2008) demonstrated that both functional forms can result from an ideal instability, with the exponential and power law indicating small and sizable perturbations of an initial equilibrium, respectively. This implies that the specific form of the main acceleration has little bearing on the debate about eruption models but rather on the magnitude of the perturbation that triggers the onset of an eruption. Some authors obtained satisfactory fits to prominence height–time data assuming uniform acceleration (e.g., Gilbert et al. 2000; Gopalswamy et al. 2003). However, this assumption implies a discontinuity in the acceleration at the onset of the main-acceleration phase, which is unphysical, and so, it only allows one to characterize this phase roughly and in a global sense. The slow rise is often found to be nearly linear (e.g., Sterling et al. 2007, 2011; Schrijver et al. 2008). Consequently, a break in characteristic behavior between the slow-rise and main-acceleration phases is indicated by the majority of the previous studies.

Quantitative investigations of whether the slow-rise and main-acceleration phases show the same or different functional forms were, to our knowledge, presented only by Kahler et al. (1988), who suggested a common power law for both, and Schrijver et al. (2008), who suggested different functions. Here, we first address the different findings by Kahler et al. (1988) and Schrijver et al. (2008) by studying the kinematics of a larger sample of 12 events observed with high resolution and at high cadence (similar to those in Schrijver et al. 2008). To account for the broad range of CME speeds, and to permit disclosing potential differences between slow and fast CMEs, we have carefully chosen six eruptions from active regions and six from the quiet Sun. The best fits of the $h(t)$ data yield a relatively precise timing of the kinematic evolution, which is then compared with the flare light curve for each event. This might either yield a discrimination between the ideal MHD and resistive eruption models, or provide information on how early and closely the feedback between flux rope instability and reconnection is established, thereby adding to the substantial existing knowledge, which has not yet established a definite picture (Zhang & Dere 2006; Maričić et al. 2007; Bein et al. 2012). Similarly, a relatively precise height of the onset of both the slow-rise and main-acceleration phases is obtained, which we utilize to determine whether one of these onsets is related to the threshold of the torus instability.

We introduce the instruments in Section 2. The criteria for choosing the sample are explained in Section 3, which is followed by the results in Section 4. The methods and results are discussed in Section 5, and the conclusions are summarized in Section 6.

2. Instruments

The data sets are mainly from the AIA on board the Solar Dynamics Observatory (SDO; Pesnell et al. 2012), which images the corona almost simultaneously at temperatures from 0.06 to 20 MK in 10 different passbands. The temporal cadence and spatial resolution are 12 s and $1''.2$, respectively. The two AIA high-temperature passbands, 131 and 94 Å, with peak responses at temperatures of ~ 11 MK and ~ 7 MK, respectively, are used for identifying hot channels and tracking their evolution in the low corona; the AIA 304 Å passband is for analyzing quiescent filaments. In order to determine the height of filaments in 3D, the EUVI 304 Å images of the Sun Earth Connection Coronal and Heliospheric Investigation (SECCHI; Howard et al. 2008) on board the Solar Terrestrial Relations Observatory (STEREO) are also utilized, although with a low cadence (10 minutes) and resolution ($2''.4$). The 720 s line-of-sight magnetograms of the full disk and daily updated synoptic maps provided by the Helioseismic and Magnetic Imager (HMI; Schou et al. 2012), also on board SDO, are taken as the bottom boundary condition for computing a 3D coronal magnetic field model by extrapolation. We also use the Large Angle and Spectrometric Coronagraph (LASCO; Brueckner et al. 1995) on board the Solar and Heliospheric Observatory to inspect the properties of CMEs. The 1–8 Å SXR flux of associated flares is provided by the Geostationary Operational Environmental Satellite (GOES).

3. Event Selection

In this study, we collect 12 eruptive events including six hot channel eruptions and six quiescent filament eruptions. Hot channels originate from active regions with strong magnetic

fields and are prone to produce fast CMEs. The visibility of the hot channels only in the AIA 131 and 94 Å passbands but not in other cooler passbands proves their high-temperature nature. Quiescent filaments are from long-time decayed active regions with weak magnetic fields and usually give rise to slow CMEs.

We select hot channels that are mostly located at or near the solar limb. The low level of background and foreground emission ensures that the edge of the hot channels is sharp enough to allow their height to be reliably tracked. The high cadence of the AIA data (compared to EUVI data) yields a large number of data points, even though the hot channels evolve rapidly. This results in the most accurate height–time data currently available, which turns out to be crucial for the reliability of the fits and the derived break points and onset heights. On the other hand, reliable magnetograms can then only be obtained 3–4 days before or after the eruptions, which affects the estimates of the decay index of the coronal field at eruption onset. Therefore, we selected only events that occurred at least several days after the emergence phase of the corresponding active regions, at which time the photospheric magnetic field evolved gradually.

The quiescent filaments are selected using the catalog compiled by McCauley et al. (2015) from a longitude range of $\pm 60^\circ$. This permits daily updates of the eruption source region in the synoptic magnetograms to be taken, which are used for the computation of the potential coronal field model. We require that the filaments have clear moving fronts during the eruption process, so that their height can be measured continuously and reliably. To allow for the true height to be determined, we only select filaments with simultaneous observations of the AIA and the EUVI from two perspectives, at least during part of the rise.

Table 1 shows the basic properties of the 12 events. One can see that all hot channel eruptions have an associated SXR flare and a corresponding CME, except the H2 event. Cheng et al. (2014b) and Tripathi et al. (2013) analyzed the H2 event in detail and found that its eruption was eventually confined by the overlying field in the high corona and, thus, did not produce a CME. However, it still experienced a slow-rise phase and then a main-acceleration process during the beginning of the eruption. From Table 1, it can also be seen that the CMEs from the hot channel eruptions do have a relatively high velocity in the range of ≈ 700 – 2100 km s $^{-1}$. For the CMEs from the quiescent filaments, the velocity is inclined to be smaller, with a range of ≈ 500 – 1400 km s $^{-1}$. Most of them lack detectable GOES SXR 1–8 Å flux, except the F1 and F5 eruptions, which produce two relatively fast CMEs with velocities above 1100 km s $^{-1}$. Overall, the velocities of the CMEs constituting our sample cover a large range of CMEs (e.g., Yashiro et al. 2006; Zhang & Dere 2006). In this sense, the results from our small sample are applicable to a broad range of events. Note that the velocity here refers to an average projected value in the LASCO field of view.

4. Results

4.1. Early Kinematics of Solar Eruptions

4.1.1. Temporal Evolution of Height, Velocity, and Acceleration

We take the hot channel H3 and quiescent filament F1 as examples to illustrate our analysis procedure. Figures 1(a) and (b) display the 131 Å image of H3 and the 304 Å image of F1, respectively. From the online, animated version of Figure 1,

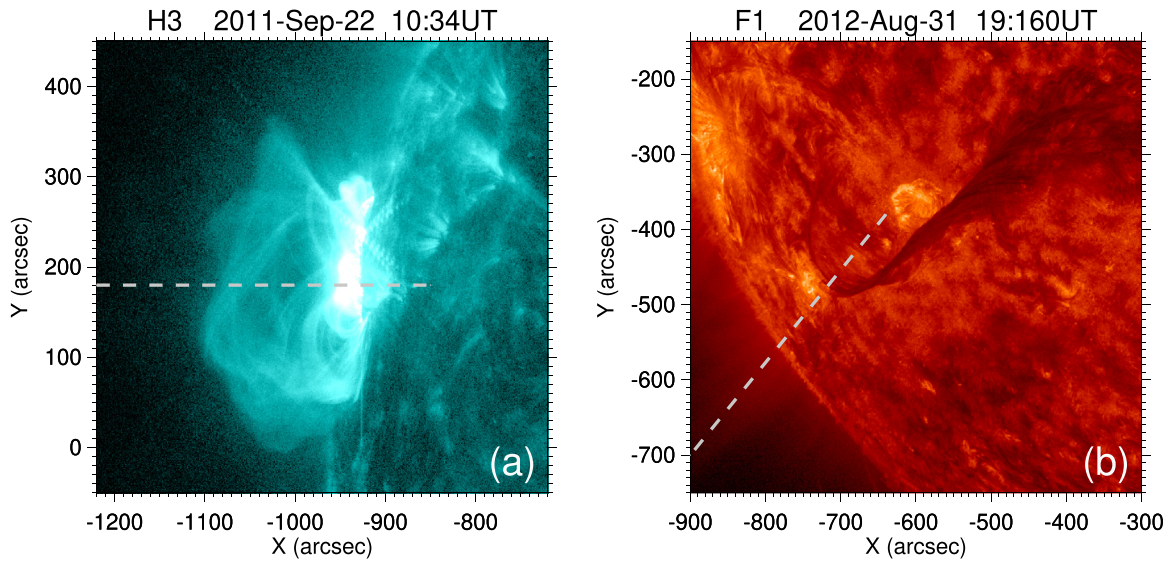


Figure 1. SDO/AIA 131 and 304 Å images showing the erupting hot channel H3 (a) and the quiescent filament F1 (b). The dashed lines indicate the direction of eruption. An animation of the SDO/AIA images is available. The 131 Å images of H3 span from 10:10 to 10:49 UT on 2011 September 22; the 304 Å images of F1 span from 18:10 to 20:00 UT on 2012 August 31.

(An animation of this figure is available.)

Table 1
CME/Flare Properties of 12 Eruption Events

Events ^a	Date	Flare ^b	Magnitude	CME ^c	Speed ^d (km s ⁻¹)	Location	References ^e
H1	2011 Mar 8	Y	M1.5	S	732	S20E75	Cheng et al. (2012, 2013b), Zhang et al. (2012)
H2	2011 Sep 12	Y	C9.9	C	...	N20E85	Tripathi et al. (2013), Cheng et al. (2014b)
H3	2011 Sep 22	Y	X1.4	S	1905	N12E85	Nindos et al. (2015)
H4	2012 Jan 23	Y	C?	S	684	N25W35	Cheng et al. (2013a)
H5	2013 May 22	Y	M5.0	S	1466	N13W80	Li & Zhang (2013b), Cheng et al. (2014a)
H6	2014 Feb 25	Y	X4.9	S	2142	S14E85	Chen et al. (2014), Seaton & Bartz (2017)
F1	2012 Aug 31	Y	C8.0	S	1442	S25E40	Wood et al. (2016), Sinha et al. (2019)
F2	2012 Nov 23	N	...	S	519	S40E15	Sinha et al. (2019)
F3	2013 Mar 16	N	...	S	786	N30W60	...
F4	2013 Aug 20	N	...	S	784	S40W00	Li et al. (2015), Sinha et al. (2019)
F5	2013 Sep 29	Y	C1.5	S	1179	N15W25	Li et al. (2015), Yan et al. (2015), Palacios et al. (2015), Sinha et al. (2019)
F6	2014 Sep 2	N	...	S	493	N25W10	Ouyang et al. (2015)

Notes.

^a H (F) refers to hot channel (quiescent filament) eruptions.

^b Y (N) denotes a detectable (not detectable) flare in the GOES 1–8 Å flux.

^c S shows successful eruptions that produce CMEs, and C denotes a failed eruption.

^d The average CME speed in the LASCO field of view obtained from <https://cdaw.gsfc.nasa.gov>.

^e Previous investigations of the event.

one can see that both H3 and F1 have a coherent structure, and their fronts can clearly be identified throughout the eruption. Quiescent filaments and prominences are most likely trapped in the dips of helical field lines, as indicated by the observations of cavities. Therefore, the magnetic axis of the erupting flux rope is best approximated by the upper edge of the erupting filament or prominence. For hot channels, the observations often suggest that they represent the erupting flux rope, whose magnetic axis should lie within the channel, roughly half way between the channel’s upper and lower edges. However, the lower edge is often difficult to determine, as Figure 1 illustrates. Therefore, we consider the upper edge of the hot channels to be the most reliable approximation of the erupting flux rope’s magnetic axis.

In order to obtain the height of H3 and F1 versus time, we make the time-slice plots as shown in Figures 2(a) and (d), respectively. The directions of the slices are chosen to ensure that the tops of H3 and F1 are crossed during most of the eruption, as indicated by the dashed lines in Figure 1. After inspecting all events in our sample, we find that their heights always present a two-phase evolution consisting of a slow-rise phase and a main-acceleration phase. Even for the failed H2 eruption, it still presents these two phases in spite of its short duration. We further examined the kinematics along different directions (within 5° from the dashed lines Figure 1) and found that such a two-phase evolution pattern always exists. In addition, we also inspect the influence of varying directions on the determination of the main-acceleration onset. This turns out

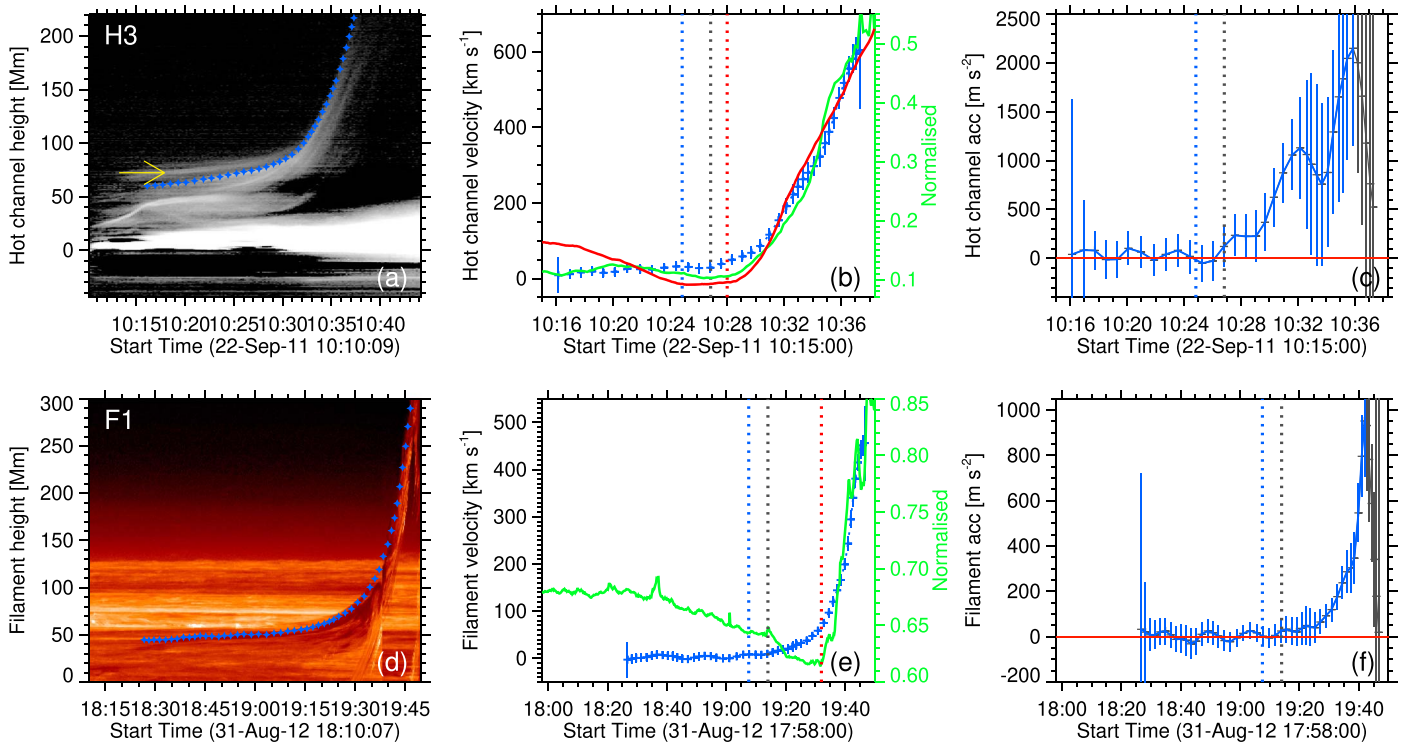


Figure 2. (a) Stack plot of the 131 Å intensity along the dashed line in Figure 1(a). The diamonds show the measured height of the continuous moving front of H3. The yellow arrow indicates the movement of nearby loops caused by the eruption of H3. (b) Temporal evolution of the velocity in the inner corona, with vertical bars showing the uncertainty in velocity. The red curve shows the GOES 1–8 Å SXR flux, and the green curve shows the source-integrated AIA 131 Å flux, which is normalized to its peak value. The flare onset (t_2) is indicated by the red vertical line. The onsets of the main acceleration of H3 determined by the fitting method and from the acceleration–time profile are shown by the two vertical lines in blue (t_3) and black (t_4), respectively. (c) Temporal evolution of the acceleration, with the dark gray data points indicating a quickly decreasing acceleration. The red horizontal line marks zero acceleration. (d)–(f) The same as panels (a)–(c) but for F1, with the green curve showing the normalized, source-integrated AIA 304 Å flux.

to be smaller than that of varying the number of height–time data points, as illustrated in Section 4.1.2.

Taking advantage of the time-slice plots, we measure the projected heights of the H3 and F1 moving fronts as shown by the diamonds in Figures 2(a) and (d), respectively. Note that another moving feature appears slightly above the upper edge of H3 during the slow-rise phase (as shown by the yellow arrow in Figure 2(a)). This is a separate structure consisting of nearby loops that were produced by a previous confined flare in the same region (see the animation of Figure 1). In order to derive the velocity, we apply the first-order numerical derivative routine `deriv.pro` from the IDL software package to the smoothed height–time (H – t) data, with a cubic spline smoothing performed by the IDL routine `IMSL_cssmooth.pro` to reduce the noise. The results are shown in Figures 2(b) and (e). Using the second-order numerical derivative, we further derive the acceleration as shown in Figures 2(c) and (f). The uncertainties in velocity and acceleration mainly stem from the uncertainty of the measured heights, which is estimated to be 2 (3) pixels for the hot channels (filaments).

Figure 2(b) shows that, during the slow-rise phase, the H3 eruption has a small, weakly accelerated rise velocity in the range 10–30 km s⁻¹. After several minutes, it starts to speed up. The velocity increases from about 50 to 600 km s⁻¹ in only 8 minutes, corresponding to an average acceleration of 1150 m s⁻². The temporal variation of the acceleration (see Figure 2(c)) shows that the acceleration is very small during the slow-rise phase. It starts to increase strongly at \sim 10:26 UT, peaks at \sim 10:36 UT, and then decreases quickly. Such a quick decrease may be due to a decreasing visibility of the structure

above the height of \sim 170 Mm (\sim 200'' above the solar limb), which is typical for hot channel eruptions, resulting in a substantial underestimate of the height. The other potential reason is a beginning saturation of the instability that drives the eruption, manifesting as a decrease of the acceleration.

Figures 2(d)–(f) show that the F1 eruption has similar height–time, velocity–time, and acceleration–time profiles to those of H3; however, the duration is much longer. It takes \sim 40 minutes for the weakly accelerated slow rise to reach a similar velocity of \sim 30 km s⁻¹. During the main-acceleration phase, the velocity varies relatively more slowly, increasing from \sim 30 to \sim 450 km s⁻¹ in \sim 30 minutes with an average acceleration of about 230 m s⁻². Figure 2(f) shows that the acceleration of F1 is also centered around zero and then starts to increase rapidly, followed by a decrease when approaching the limit of the AIA field of view. It is worth mentioning that the projection effect has a significant influence on the measured heights, velocities, and accelerations of the quiescent filaments but not on the character of their temporal profiles. We will estimate the true heights in Section 4.3. Moreover, for both hot channels and quiescent filaments, the solar rotation has some contribution to the velocity, which is, however, very small (< 1 km s⁻¹) and can be neglected (McCauley et al. 2015).

4.1.2. Fit of Height–Time Profiles

In order to infer the functional forms of the slow-rise and main-acceleration phases and a possible break point between them, we consider a set of fit functions for the measured height–time profiles. A nonlinear function is required to fit the

main-acceleration phase; here, we include the exponential and the power law, as suggested by previous work (see Section 1). We do not include the often-used tanh function (e.g., Sheeley et al. 2007) because this extends the fitting into the propagation phase after the main acceleration, which is beyond the scope of the present investigation. Moreover, a linear or quadratic function appears appropriate for the slow-rise phase, as the acceleration in this phase is typically *much* weaker (Figure 2). A constant term includes the initial height for each event. In order to determine whether a break point exists, we compare the nonlinear fit functions with a superposition of the nonlinear and the linear or quadratic functions. The superposition should yield the better fit in the presence of a break point. The application of each fit function to the whole time series for each event ensures comparability between the fits, because the measure of goodness, the reduced chi-squared, χ_ν^2 , is then based on the same number of data points for each fit function.

The fit is performed for the main part of the height–time profiles including all measured heights up to the final point of increasing acceleration. This is consistent with the character of all fit functions, which do not include a decreasing second derivative. In trying to fit the superposed functions to the data, it is found that the fitting software often cannot find a better fit when the quadratic term is included. In some cases, a poorer fit than that excluding the quadratic term is obtained; although, a vanishing coefficient for this term would be a valid solution, providing a very similar goodness of fit as the superposition with the linear function. In the interest of using a uniform method for all events, we have, therefore, dropped the quadratic term. This aspect is elaborated further by applying the quadratic fit function (including the linear term) only to the slow-rise phase that is inferred from the superposed fit. It turns out that the uncertainty of the acceleration is bigger than, or comparable to, the inferred acceleration for six of the 12 events (see detail below). This additionally suggests that the fitting of the slow-rise phase to a linear function should be restricted; although, the velocity data show a small increase in this phase for several of our events. Thus, the following functions are employed in the fitting:

$$h_1(t) = a_1 \exp(b_1 t) + d_1, \quad (1a)$$

$$h_2(t) = a_2 \exp[b_2(t - t_0)] + c_2 t + d_2, \quad (1b)$$

$$h_3(t) = a_3 t^{b_3} + d_3, \quad (1c)$$

$$h_4(t) = a_4(t - t_0)^{b_4} + c_4 t + d_4, \quad (1d)$$

where h_i and t denote fitting height and time, respectively. The quantities a_i , b_i , c_i , d_i , and t_0 are the coefficients of the functions to be determined by the fit. The fit is performed by the routine `mpfit.pro` (Markwardt 2009), which is available in the Solar SoftWare (SSW) package. The reduced chi-square χ_ν^2 is calculated by $\frac{\chi^2}{N-m}$, where $\chi^2 = \sum_{i=1}^N \frac{[h_i(t) - H_i(t)]^2}{\sigma_i^2}$, N denotes the number of data points, $N - m$ is the number of the degrees of freedom, i.e., the number of data points minus the number of free parameters (m) in the fit function, and σ_i is the error for each measured height $H_i(t)$. The best fit is indicated when χ_ν^2 is closest to unity.

For the nonlinear component of the superposed functions, we employ a two-step strategy. First, to minimize the difference between the purely nonlinear and the superposed fit functions, we set $t_0 = 0$. This allows us to compare the resulting fits on the formally most equal basis but implies the assumption that

the nonlinear evolution of the rise commences simultaneously with the slow rise (our first data point). Since we also intend to address the question of whether the nonlinear evolution (indicating onset of instability) starts off associated with the slow rise or with the main acceleration, we treat t_0 as a free parameter in a second step.

The results for H3 and F1 are shown in Figure 3. One can see that all functions can fit the height–time profiles relatively satisfactorily, but the goodness of fit can be obviously distinguished in the velocity–time profiles. This is also apparent for most of the other events, shown in Figures 4 (hot channels) and 5 (quiescent filaments). The existence of a different functional form, hence the existence of a break point, between the slow-rise and main-acceleration phases is demonstrated by the clear superiority of the χ_ν^2 values for one or both of the superposed functions $h_2(t)$ and $h_4(t)$ for all 12 events (Table 2). Additionally, the exponential fit is superior to the power-law fit for the majority of our events (three of the six hot channel eruptions and all six quiescent filament eruptions). For each event, we obtain an estimate of the break-point time where the velocity of the nonlinear term starts to take over (equals) that of the linear term in the best-fitting superposed function, $h_2(t)$ or $h_4(t)$. This time is given as t_3 in Table 3. It has an uncertainty that we estimate by excluding a varying number of the first or final data points from the best fit. The uncertainty of the break point is estimated to be within ~ 4 minutes for the hot channels and ~ 10 minutes for the quiescent filaments.

Next, the superposed fits are repeated allowing for a nonzero onset time of the nonlinear evolution, $t_0 \geq 0$. It turns out that the shape and χ_ν^2 value of the best fit are nearly identical to the fit with prescribed $t_0 = 0$, but most resulting fit values for the onset time t_0 strongly precede the break-point times t_3 , especially for the quiescent filaments; see Table 3. Comparing the inferred value for t_0 with the shape of the velocity–time profile, it can be seen in Figures 3–5 that t_3 appears to be a far more reliable estimate of the onset of the main acceleration than t_0 for most events. Therefore, we will not use the inferred onset times t_0 in further analyses. One should be aware that the main acceleration may start somewhat earlier than t_3 because it needs some time to build up a velocity comparable to the slow-rise velocity. For a rough estimate of this time, we adopt the assumption that the main acceleration starts from near the time t_s where the nonlinear velocity component satisfies $v(t_s) = v(t_3)/10$; the value of t_s is also listed in Table 3.

In order to further validate our judgment with regard to excluding the quadratic term, we only fit the data points in the slow-rise phase, before the inferred break point t_3 , with the linear and linear-plus-quadratic functions. The results are shown in Figure 6. One can see that the linear fit is generally very close to the quadratic one. Only H1, H3, and H5 show a significant average acceleration, which is moderate only for H1, and is otherwise small. H4, F2, F4, and F6 also obtain a valid acceleration; however, the value is extremely small ($< 0.5 \text{ m s}^{-2}$). For the other events, the uncertainty of the inferred acceleration is bigger than the acceleration itself, which appears to be due to a small number of data points (H2, H6) or an oscillatory behavior of the slow-rise velocity and acceleration (F1, F3, F5).

From the break point t_3 and our first data point for the slow-rise phase, we obtain its duration, which is shown by D in Table 3 and Figure 7(a). One can see that the duration of the slow-rise phase for CMEs from the hot channel eruptions is

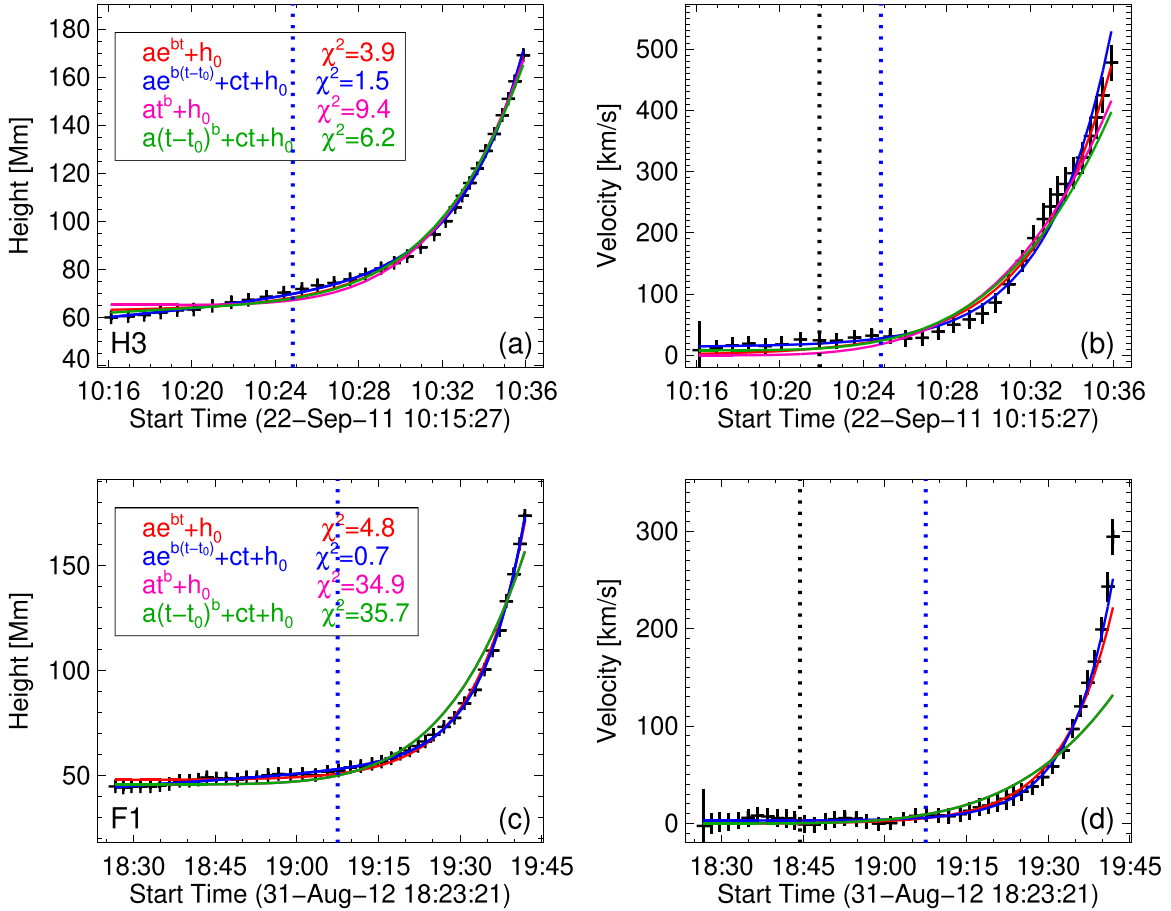


Figure 3. Model fitting of the rise profile for H3 (a)–(b), and F1 (c)–(d). The green, red, blue, and pink lines show the fitting results of the four functions as shown in the top left corner of panels (a) and (c). The blue vertical lines indicate the onset time t_3 of the main acceleration obtained from the best fit of $h_2(t)$ with prescribed $t_0 = 0$, and the black vertical lines show the resulting t_0 when it is included as a free parameter, $t_0 \geq 0$, in the fit.

mostly much shorter than that of the erupting filaments. The latter all have a slow rise of >40 minutes and up to >170 minutes for F4–F6. The H4 event also has a slow-rise phase of long duration (~ 75 minutes). As noted already above, a long and high hot channel connecting the periphery of the two active regions erupts in this event, so that the corresponding magnetic field strength is much weaker than that of the other five hot channels, which originate from the central area of their active regions. This resembles the quiescent filaments that originate from large-scale and weak magnetic flux.

4.2. Timing Relation to Flares

4.2.1. Main-acceleration Phase

We compare the early kinematic evolution of the eruptions with the evolution of the associated flare emission. Figure 2(b) shows that the velocity evolution of H3 is closely synchronized with the GOES 1–8 Å SXR light curve during the main part of the main-acceleration phase. Since the GOES flux is from the full disk and may include a contribution from other regions, we also integrate the AIA 131 Å intensity in the H3 source region to represent the flare emission of the event. The velocity evolution is even somewhat better synchronized with the evolution of the integrated AIA 131 Å flux. Except for H4, such a simultaneity is also true for the other hot channel events, although not always tightly close (e.g., the H1 event, Figure 4). The exception of H4 is mainly due to the fact that it originates

from a large-scale magnetic structure that connects two nearby active regions, whereas the GOES flux is from two successive flares occurring at two different locations in the active-region complex (Cheng et al. 2013a).

For the quiescent filaments, we utilize the 304 Å intensity as the proxy of the associated flare emission because the relevant ribbons and arcades only clearly appear in the AIA low-temperature passbands but not in SXR and AIA high-temperature passbands. These flares are usually very weak, with the plasma not being heated above a temperature of ~ 10 MK (the peak temperature of the 131 Å response function). We also inspect the 171 and 211 Å fluxes and find that their profiles are very similar to that of the 304 Å flux. Similar to the hot channels, the velocity evolution of the erupting filaments keeps in step with the evolution of the integrated AIA 304 Å flux in the main-acceleration phase (Figures 2(e) and 5). Again, the synchronization is not tight in some events (F2 and F3). Overall, this indicates that the mechanism of the main CME acceleration and the mechanism of the rapid increase of the flare emission are coupled, often closely, for both hot channels and quiescent filaments during the main part of the energy release in the eruptions.

4.2.2. Slow-rise Phase

The velocity evolution of the hot channels shows some synchronization with the temporal variation of the integrated AIA 131 Å flux also during the slow-rise phase (except H4).

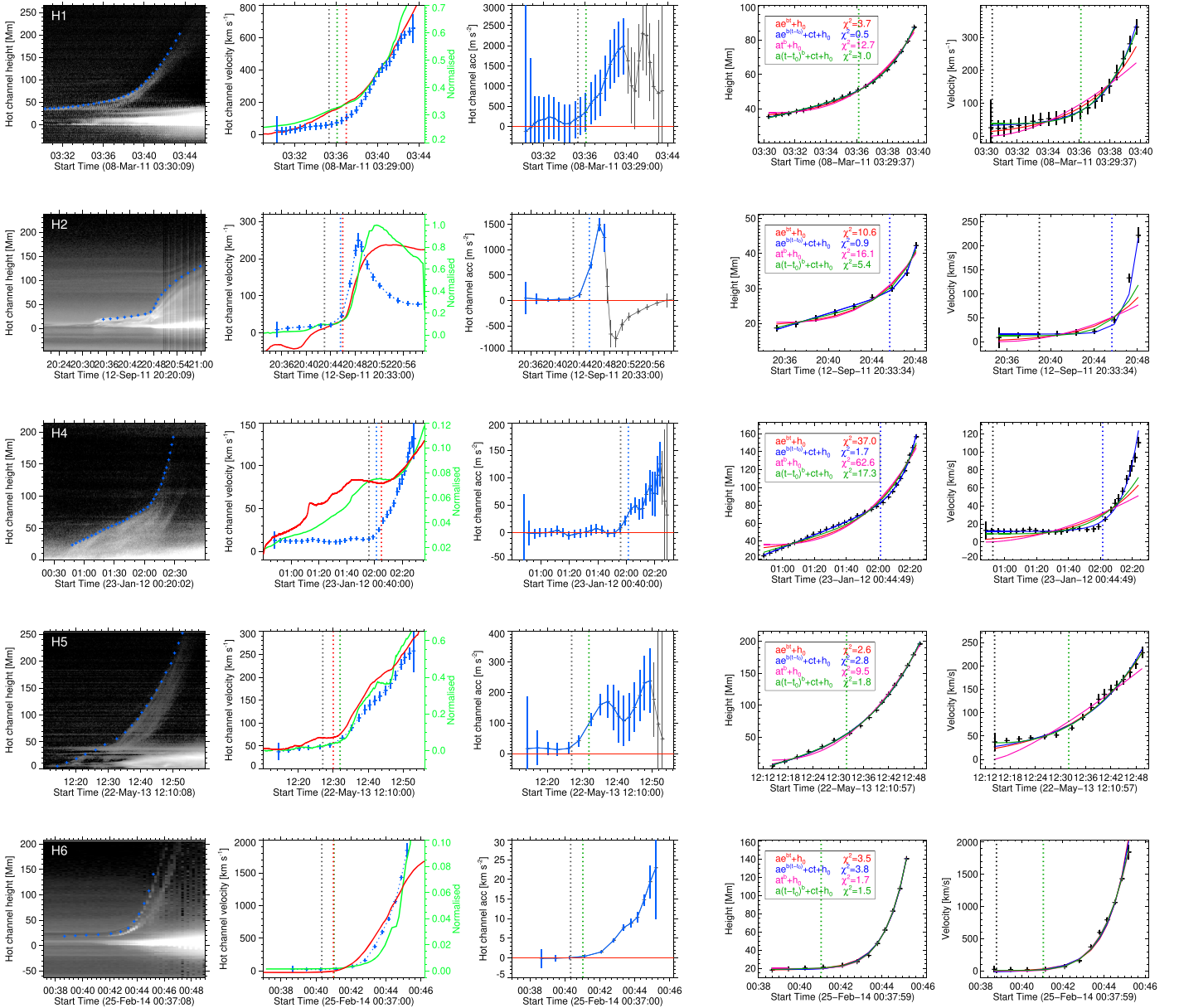


Figure 4. The same as Figures 2 and 3 but for H1, H2, and H4–H6.

Both tend to show a slow rise in roughly the same time interval, with the evolution being quite close for some events (H2, H5, and H6). However, two very different types of evolution are seen for the filaments. The integrated AIA 304 Å flux of F2–F4 slowly increases, quite well synchronized with the slow rise of the filament velocity, similar to the hot channels. For the other three events, the integrated AIA 304 Å flux decreases with time, which is due to a spreading of the erupting filament material to cover a larger area, thus resulting in more absorption. However, through carefully examining the 304, 171, and 211 Å images, we find some EUV bright points or small-scale brightenings that appear near the barbs of, or underneath, all slowly ascending filaments, indicating a related occurrence of reconnection. Such brightenings can even appear for a long time prior to the beginning of the slow-rise phase. The time of the first detected brightening is shown as t_1 in Table 3. The brightenings are not visible in the integrated EUV flux curves because they are small, and their flux changes

slowly. This indicates that the underlying reconnection evolves at small scales and in a gentle way, as expected for slow tether-cutting reconnection.

4.2.3. Onset Time

Next, we compare the onset times of the CME main-acceleration and impulsive flare phases. In the NOAA reports, the flare onset time is defined as the first minute in a sequence of 4 minutes of successive increase in the GOES 1–8 Å SXR flux. Here, we obtain the onset time by carefully inspecting the temporal variation of the 1–8 Å SXR flux, using the criterion that, from this time onward, the flux increases continuously and far more rapidly than before. For H1 and H6, the 15–25 keV hard X-ray flux from RHESSI is also utilized, using the same criterion (for H1 see Figure 10 in Cheng et al. 2013b). The onset of the flares associated with the quiescent filaments is determined using the same strategy, with the integrated AIA 304 Å flux replacing the 1–8 Å SXR flux. The results are

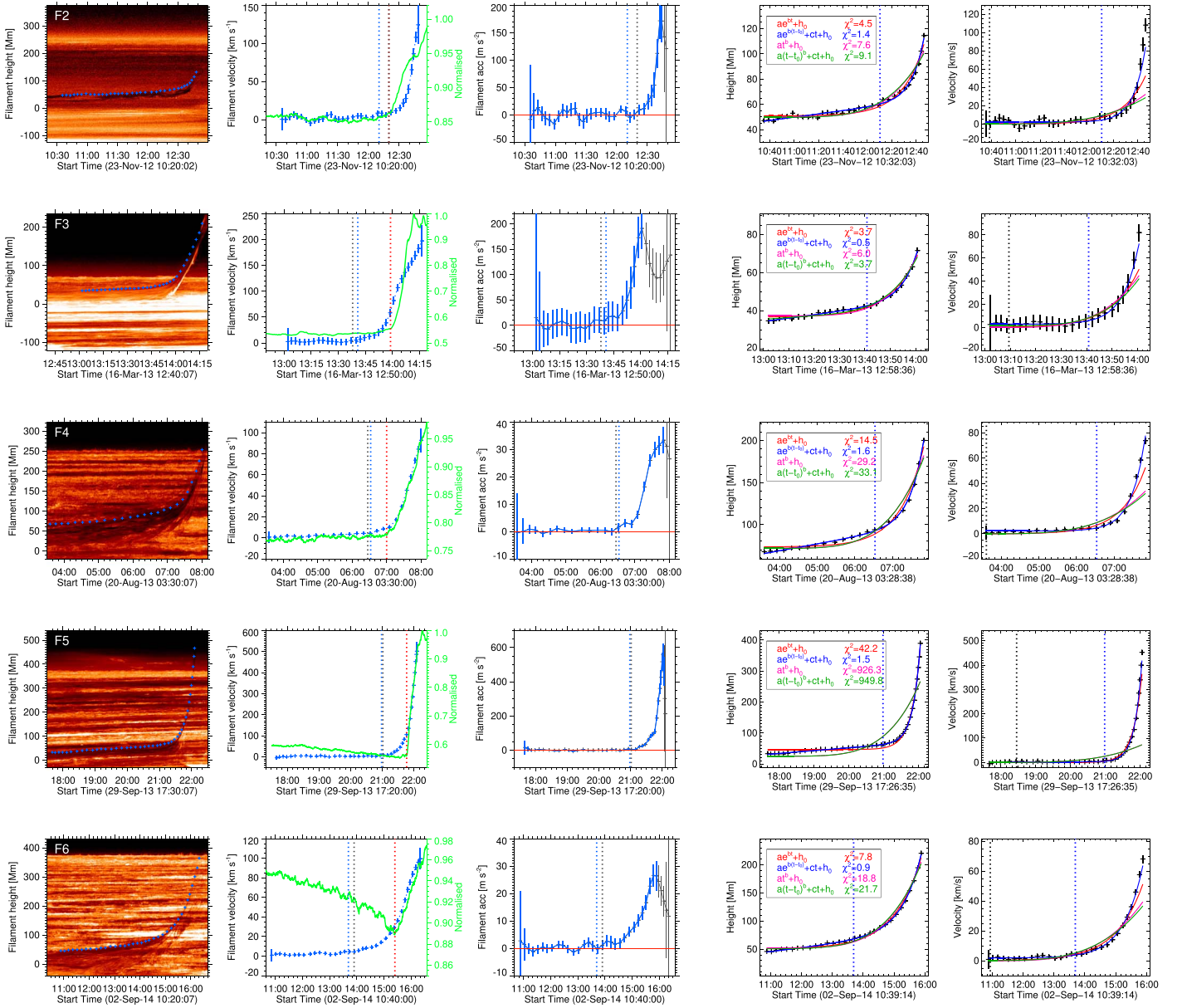


Figure 5. The same as Figures 2 and 3 but for F2–F6.

Table 2
Metrics for Fitting Goodness of Different Functions

Events	$a_1 e^{b_1 t} + d_1$ $\chi^2_{\nu 1}$	$a_2 e^{b_2(t-t_0)} + c_2 t + d_2$ $\chi^2_{\nu 2}$	$a_3 t^{b_3} + d_3$ $\chi^2_{\nu 3}$	$a_4 (t - t_0)^{b_4} + c_4 t + d_4$ $\chi^2_{\nu 4}$
H1	3.7	0.5	12.7	1.0
H2	10.6	0.9	16.1	5.4
H3	3.9	1.5	9.4	6.2
H4	37.0	1.7	62.6	17.3
H5	2.6	2.8	9.5	1.8
H6	3.5	3.8	1.7	1.5
F1	4.8	0.7	34.9	35.7
F2	4.5	1.4	7.6	9.1
F3	3.7	0.5	6.0	3.7
F4	14.5	1.6	29.2	33.1
F5	42.2	1.5	926.3	949.8
F6	7.8	0.9	18.8	21.7

Table 3
Properties of Early Kinematics of 12 Eruption Events

Events	t_1 (UT)	t_2 (UT)	t_0 (UT)	t_3 (UT)	t_s (UT)	δt_{32} (minutes)	t_4 (UT)	δt_{42} (minutes)	D (minutes)	v (km s ⁻¹)	a (m s ⁻²)	h_c (Mm)	n_c	h_0 (Mm)	n_0
H1	03:28	03:37	03:30	03:36	03:34	-1	03:35	-2	5	39.5 ± 2.9	157.7 ± 73.7	50	1.60 ± 0.03	36	1.37 ± 0.04
H2	20:30	20:46	20:39	20:46	20:44	0	20:43	-3	11	16.2 ± 1.9	24.6 ± 25.8	29	1.46 ± 0.08	19	1.06 ± 0.10
H3	09:00	10:28	10:22	10:25	10:18	-3	10:27	-1	9	20.6 ± 1.6	39.7 ± 24.3	70	1.88 ± 0.03	60	1.69 ± 0.04
H4	00:30	02:05	00:52	02:01	01:38	-4	01:56	-11	75	12.7 ± 0.1	0.4 ± 0.2	124	1.68 ± 0.18	36	1.08 ± 0.46
H5	12:15	12:30	12:14	12:32	12:21	2	12:27	-3	18	45.1 ± 1.7	19.8 ± 13.7	54	1.57 ± 0.10	5	0.21 ± 0.12
H6	00:20	00:41	00:39	00:41	00:40	-0	00:40	-1	2	22.7 ± 12.9	-80.6 ± 934.3	21	1.57 ± 0.34	18	1.46 ± 0.47
F1	17:20	19:32	18:44	19:08	18:50	-24	19:14	-18	43	3.1 ± 0.3	-0.9 ± 1.1	120	1.51 ± 0.24	101	1.34 ± 0.27
F2	09:40	12:20	10:38	12:10	11:47	-10	12:20	-0	97	1.9 ± 0.1	0.4 ± 0.2	100	1.00 ± 0.40	79	0.89 ± 0.35
F3	13:00	13:59	13:09	13:41	13:27	-18	13:38	-21	40	3.1 ± 0.5	-0.2 ± 1.8	50	1.05 ± 0.56	40	0.86 ± 0.53
F4	04:00	07:00	03:36	06:32	05:41	-28	06:27	-33	188	2.4 ± 0.1	0.3 ± 0.0	180	1.25 ± 0.23	131	1.04 ± 0.24
F5	17:00	21:46	18:27	20:59	20:30	-47	21:01	-45	202	2.5 ± 0.0	0.0 ± 0.0	120	1.42 ± 0.16	63	0.75 ± 0.13
F6	11:30	15:24	10:56	13:41	12:15	-103	13:54	-90	171	2.0 ± 0.1	0.1 ± 0.0	140	0.92 ± 0.11	95	0.75 ± 0.14

Note. t_1 denotes the time of the first appearance of EUV brightenings, t_2 refers to the onset time of the GOES 1–8 Å flux (integrated AIA 304 Å flux) of flares associated with hot channel (quiescent filament) eruptions, t_0 is the onset time of the exponential component ($h_2(t)$) or power-law component ($h_4(t)$) (see the text for its relevance), t_3 is the break point between the linear and nonlinear rise, approximating the onset time of the main acceleration. t_s is the time where the exponential component velocity $v(t_s) = v(t_3)/10$, δt_{32} denotes $t_3 - t_2$. t_4 is the onset time estimated directly from the acceleration–time profile, δt_{42} denotes $t_4 - t_2$. D and v are the duration and linear velocity of the slow-rise phase, a is the acceleration of the quadratic fit. h_0 and h_c are the initial and critical height at the onset time of the slow-rise and main-acceleration phases (t_3), respectively. n_0 and n_c are the corresponding decay index values of the extrapolated background field.

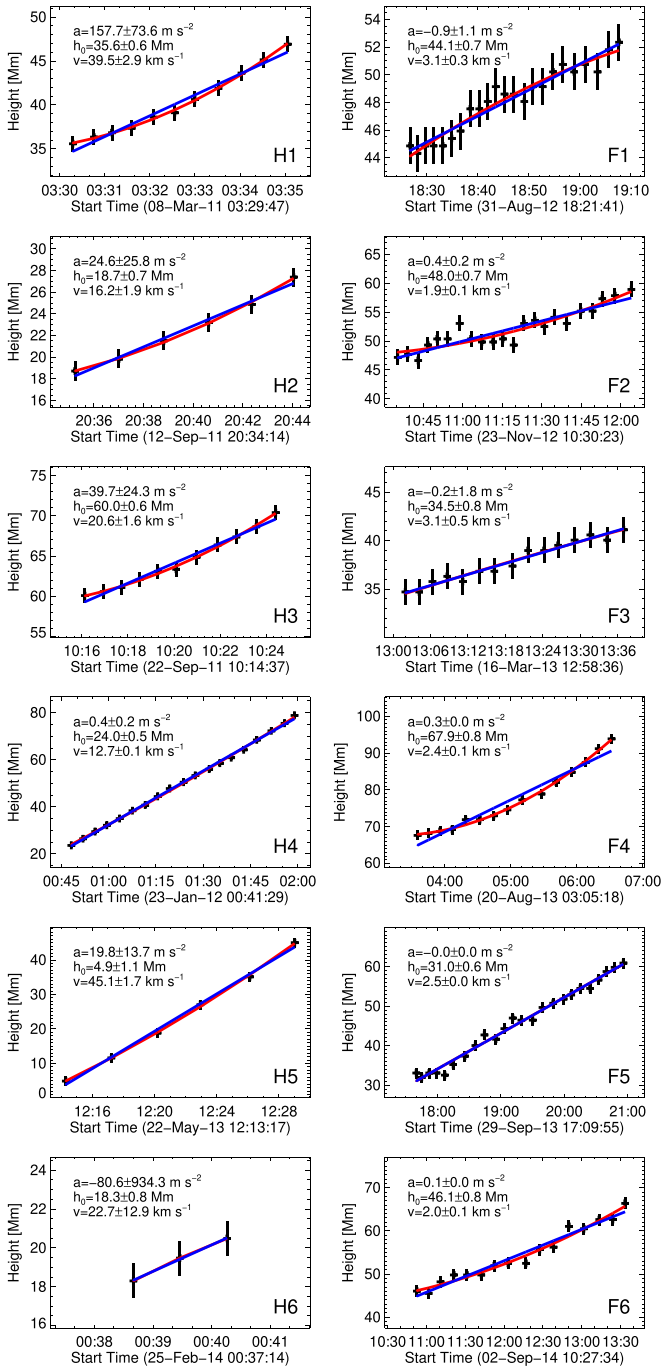


Figure 6. Linear (blue) and linear-plus-quadratic (red) fit to the slow-rise phase of all eruptions.

shown as the red vertical lines in Figures 2, 4, and 5 and are also listed as t_2 in Table 3. The onset time of the main acceleration is approximated by the break point t_3 of our best fit with $t_0 = 0$. In addition, we also estimate the main-acceleration onset directly from the acceleration–time profiles as the time when the acceleration starts to increase continuously and with a magnitude larger than the standard deviation of the acceleration during the slow-rise phase; this time is shown by the black vertical lines in Figures 2, 4, and 5, and it is listed as t_4 in Table 3. The half period of the oscillations in the slow-rise phase may serve as a rough estimate of the uncertainty of the t_4

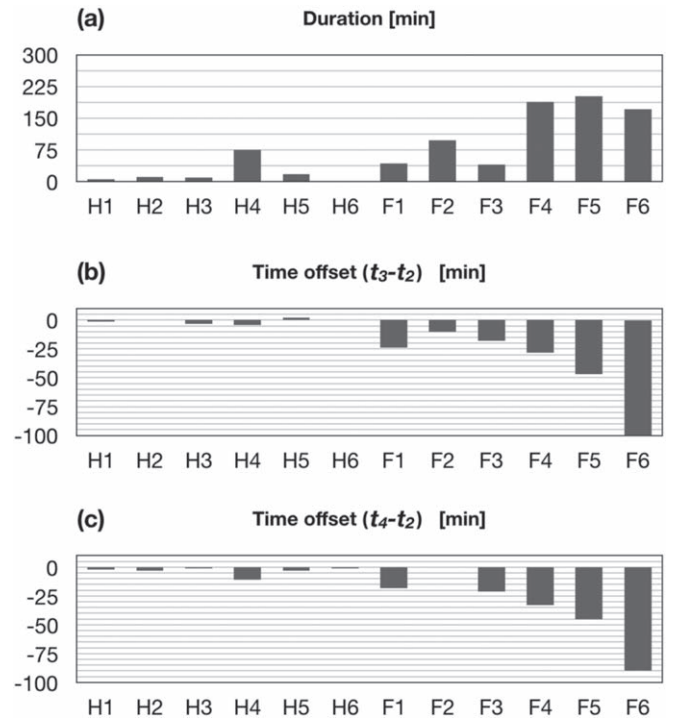


Figure 7. (a) Distribution of the duration of the slow-rise phase. (b), (c) Distributions of the temporal offset between the onset of the main acceleration and the associated impulsive flare; negative values indicate a delayed flare.

values, with the true onsets occurring earlier (not later) than t_4 . The uncertainty lies in the range of 1–4 minutes for the hot channels (~ 8 minutes for H4) and 5–25 minutes for the quiescent filaments, comparable to the uncertainties of t_3 . Similarly, the true onset of the impulsive flare is masked by precursor activities in the slow-rise phase of several events and occurs before the listed values of t_2 , with an uncertainty comparable to that of t_4 (or bigger in complex events like H4 and H1).

We then calculate the time difference between the main-acceleration onset and the flare onset ($\delta t_{32} = t_3 - t_2$ and $\delta t_{42} = t_4 - t_2$) as shown in Table 3 and Figures 7(b) and (c). It is found that the main-acceleration onset times derived from the fit (t_3) and from the acceleration–time profile (t_4) are very close to each other, except for H4. The difference to the flare onset time from both estimations is found to be close to zero (with a scatter of 3 minutes, which is smaller than the estimated uncertainty of 4 minutes for t_3) for the other five hot channel events. Note that the H4 event has no synchronization in the slow-rise phase and has the poorest synchronization of all events in the main-acceleration phase. However, for most of the quiescent filaments, the onset of the main acceleration occurs much earlier than that of the flare. The indication of a delayed flare onset is weak (δt_{32} comparable to the uncertainty of t_3) only for F2. For the other erupting filaments, the delay clearly exceeds the estimated uncertainty of t_3 (~ 10 minutes) and also the uncertainty of t_4 for each event, and it even reaches ≈ 100 minutes for F6. These large delays indicate that the mechanism that initiates the impulsive rise of the associated flare (fast “flare reconnection”) cannot be the mechanism that initiates the main acceleration of the erupting quiescent filaments.

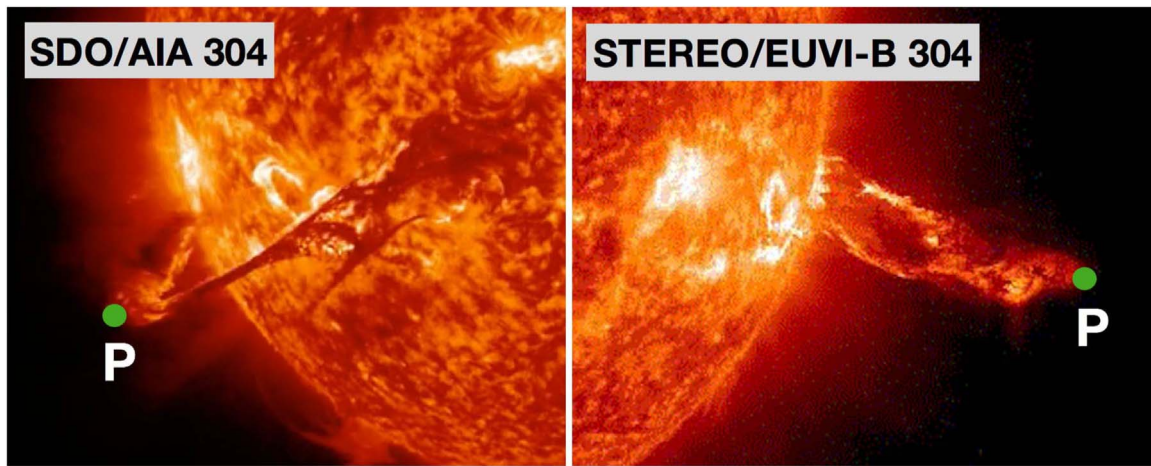


Figure 8. SDO/AIA 304 Å and STEREO/EUVI 304 Å images showing the erupting quiescent filament F1 as observed from two perspectives. The point P represents the same feature, identified to determine the location of the filament top in 3D at 19:45 UT on 2012 August 31.

4.3. Relevance of Torus Instability

To investigate the relevance of the torus instability in initiating solar eruptions, we compare its theoretical threshold (critical decay index of the background/strapping field) with the observationally estimated values at the onset of our events. The decay index is defined as

$$n(h) = -\frac{d(\ln B_t)}{d(\ln h)}, \quad (2)$$

where B_t is the horizontal component of the coronal background field. For the observational estimate, the critical (i.e., onset) height and a coronal magnetic field model are required. Different methodological approaches are possible for each of them, e.g., the different fit functions used in Section 4.1 and different extrapolation schemes. Moreover, the lack of magnetic measurements from STEREO enforces adopting a compromise between the accuracy of the height–time and magnetic measurements. Accordingly, we have chosen different strategies for the hot channel and quiescent filament eruptions, as detailed in the following. Their respective advantages and limitations are discussed in Section 5.4.

First, we address the onset of the main-acceleration phase, using t_3 from the best height–time fit for each event as the onset time. For the hot channel eruptions, we use the corresponding height projected in the plane of sky as the critical height h_c , but reference it to a point in the middle of the associated flare ribbons or at the bottom of the flare loops (Figures 1(a) and 2(a)). Except for H4, the hot channels are sufficiently close to the limb to give a negligible difference between the projected and radial distances to the reference point. The projected height of H4 is corrected assuming a radial direction of the eruption.

For the quiescent filaments, the critical heights are estimated through observations from two perspectives. We use the routine `scc_measure.pro` in the `SSW` package, which returns the location of the filament top in 3D, including its true height, latitude, and longitude. Figure 8 illustrates the 3D position measurement for the top section of F1. Figure 9 shows the evolution of the true heights for F1–F4. The critical heights of the F1, F3 and F4 eruptions are directly determined at the onset time, t_3 , of the main acceleration. For the F2 and F5 eruptions, they are estimated through a backward extrapolation

from the first 3D height point to the onset time, assuming a linear velocity in the early part of the main-acceleration phase not covered by STEREO data and with the projection effects corrected using the true eruption direction. For F6, with only two frames of the eruption captured by STEREO, the projection correction is done assuming that the eruption is along the radial direction.

The relevant (external poloidal) component of the coronal background field is approximated by a potential-field extrapolation from the best available magnetogram. We consider the Green function method to be most appropriate at the rather small onset heights of the hot channel eruptions H1–H3, H5, and H6 and the potential-field source-surface model (PFSS; Schatten et al. 1969), which includes the influence of the heliospheric current sheet, to be most appropriate at the much larger onset heights of the quiescent filament and H4 eruptions.

For both groups of events, the magnetogram data necessarily contain measurements partly or fully taken at times shifted from the eruptions. This problem is more severe for our five hot channel eruptions at or near the solar limb (i.e., except H4). Their boundary data are taken 3–4 days before or after the eruptions. Our selection of events solely from active regions at least several days after their emergence phase minimizes the effect of magnetogram evolution during this period. Additionally, we argue that it is the large-scale structure of the source region that is most relevant for the determination of the decay index at the typical onset heights (see Section 5.4), and the large-scale structure does not show strong changes during the relevant period for any of our hot channel events. The specific evolution of the source regions can be seen in Figure 10. For H1 and H5, all changes in the magnetogram (emergence, shearing, dispersal, and cancellation of flux) are very minor. For H2, H3, and H6, significant flux cancellation occurs in the center of the active regions, but the main flux concentrations contributing the background field evolve only moderately, with the large-scale structure, in particular their distance, changing weakly. Therefore, we consider the inferred critical decay index values to provide a reasonable approximation of their true values. The deviations from the true decay index values are likely to increase the range found in our sample of hot channels, but they are not likely to introduce a false systematic trend, which could strongly affect the average value. This is supported by the fact that the inferred decay index values for

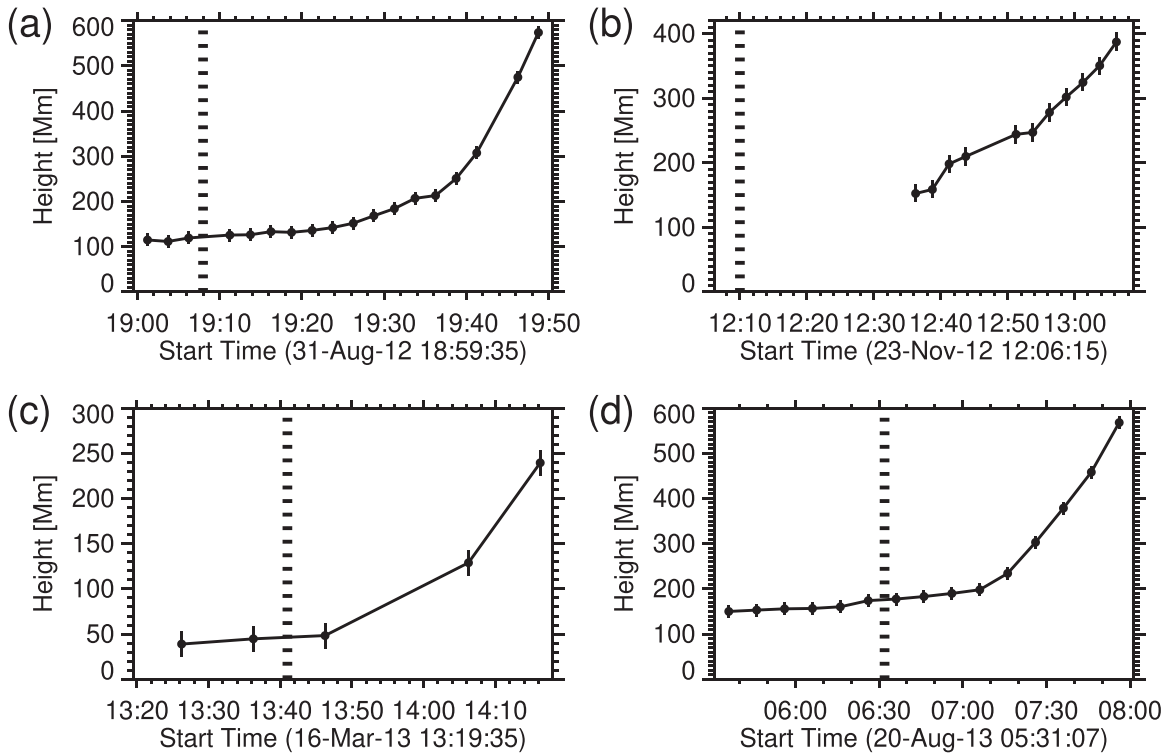


Figure 9. True (3D) height of the erupting filaments F1–F4 vs. time. The vertical lines denote the onset time of the main acceleration, t_3 , with the horizontal width denoting the uncertainty.

H1 and H5, which show the slowest magnetogram evolution, lie very close to the average value for all hot channels (see below and Table 3). We base our conclusions on the average values for the two groups of eruptions.

For the quiescent filaments and H4, we use daily updated synoptic maps as the bottom boundary condition; here, a 60° longitudinal window is updated using the average of 20 magnetograms from the same day (Sun 2018). All our quiescent filament eruptions originated from within this longitude range. Therefore, the magnetogram information for part or all of the sources of the background field is updated daily. The above general arguments in favor of the meaningfulness of the derived decay indices for the hot channels, especially of their average value, apply here as well.

The results for H3 and F1 are shown in Figure 11. Panels (a) and (b) display the distributions of the vertical magnetic field component at the height of $1.1 R_\odot$. We determine the relevant section of the main polarity inversion line (PIL), shown by the dotted lines, at this height in the middle of our eruption onset heights, rather than at the photospheric level. Panels (c) and (d) show the decay index versus height, averaged along the relevant section of the PIL. The inferred critical heights (h_c) and corresponding decay index values (n_c) for all events are compiled in Table 3 and Figures 12(a) and (b). The decay index errors are the standard deviations of all decay index values above the selected pixels along the PIL.

From Table 3 and Figure 12(a), one can see that the critical heights for the hot channel eruptions are distributed in the range of 21–83 Mm with an average of 50 Mm, which is systematically smaller than those for the quiescent filament eruptions, 50–180 Mm with an average of 118 Mm. This corresponds to different spatial scales of the main flux concentrations in the photospheric boundary. However, the decay indices at the critical heights for the former, ranging from 1.46 ± 0.08 to

1.88 ± 0.03 with an average \bar{n}_c of 1.6 ± 0.1 , are systematically greater than those for the latter, which fall in the range of 0.92 ± 0.11 – 1.51 ± 0.24 with an average \bar{n}_c of 1.2 ± 0.2 (Figure 12(b)). These decay indices for the hot channels are close to the threshold of the torus instability for the circular flux rope (1.4–1.9; Török & Kliem 2005; Kliem & Török 2006; Fan & Gibson 2007; Aulanier et al. 2010), and the values for the quiescent filaments are comparable with the threshold of the torus instability for the straight flux rope (1.1–1.3; Démoulin & Aulanier 2010).

The initial heights (h_0) and resulting decay index values (n_0) at the onset of the slow-rise phase tend to be subcritical, as can be seen in Table 3 and Figures 12(c) and (d). For the hot channels, the initial height represents the height where they can first be identified obviously. For the filaments, the initial height is deprojected using the expression $h_0 = h_c h_{p0} / h_{pc}$, where h_{p0} and h_{pc} are the projected heights at the first and break point, respectively. We find that the initial heights yield clearly lower decay index values in the ranges $n_0 = 0.21 \pm 0.12$ – 1.69 ± 0.04 ($\bar{n}_0 = 1.1 \pm 0.5$) for the hot channels and $n_0 = 0.75 \pm 0.14$ – 1.34 ± 0.27 ($\bar{n}_0 = 0.9 \pm 0.2$) for the quiescent filaments. The averages clearly fall below the instability threshold. It is worth noting that these are upper limits for both the onset heights and corresponding decay indices, because the slow-rise phase might actually commence before the first measured data point (e.g., Xing et al. 2018).

The inferred decay index values, in particular, their averages, suggest that the main-acceleration phase commences by the onset of the torus instability. This also naturally explains the initially exponential evolution of the acceleration in this phase for the majority of the events and is consistent with the power-law evolution for the remaining events (Schrijver et al. 2008). In comparison, the onset of the slow-rise phase by ideal MHD instability, as considered in Zhang & Dere (2006), see their

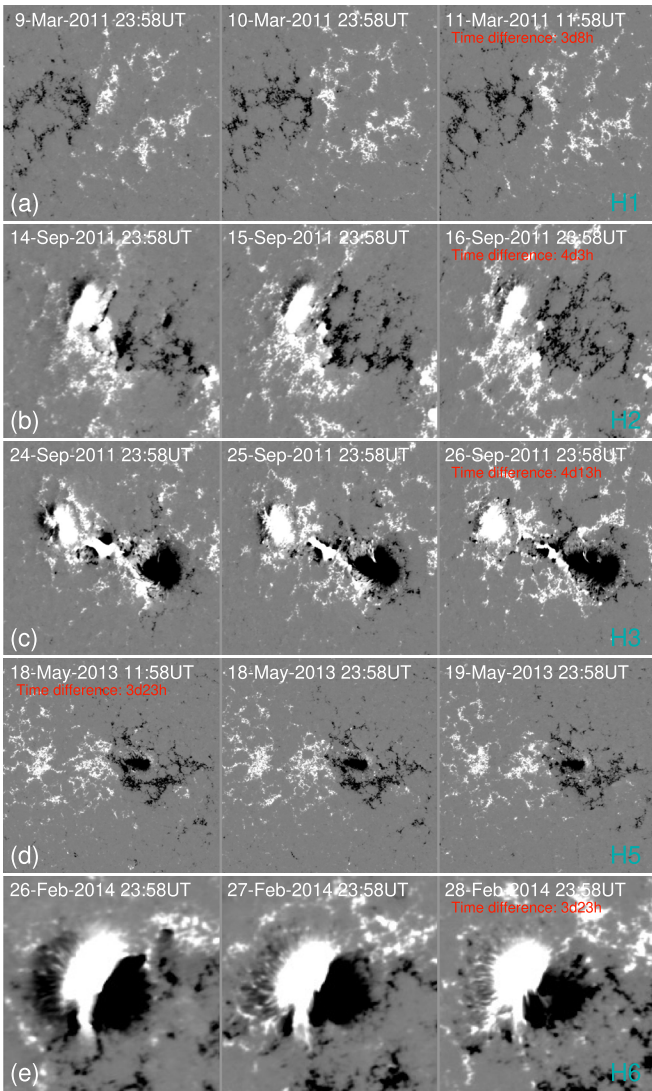


Figure 10. HMI line-of-sight magnetograms showing the evolution of the source region magnetic field of H1, H2, H3, H5, and H6 during the period of 3–4 days. The magnetograms used for calculating the background field and its time intervals with the eruptions are also indicated by the time difference in red.

Figure 1, is much less supported because the corresponding decay index values mostly lie below 1.1, which is the smallest threshold derived so far for the torus instability (Démoulin & Aulanier 2010).

5. Discussion

5.1. Early Kinematics

In this paper, we study the initiation and early kinematic evolution of 12 solar eruptions including six active-region hot channel eruptions and six quiescent filament eruptions. The 12 events produce 11 CMEs with a wide velocity distribution, ranging from $\sim 500 \text{ km s}^{-1}$ (for F2 and F6) to $\sim 2000 \text{ km s}^{-1}$ (for H3 and H6); their height–time profiles, though, do not differ qualitatively. This indicates that the basic two-phase initial kinematic evolution of CMEs may be uniform in character for most events, largely irrespective of the details of the pre-eruptive configuration.

All eruptions studied here exhibit a slow-rise phase followed by a main-acceleration phase, similar to the previous results

derived from EIT and LASCO data at low cadence (e.g., Neupert et al. 2001; Zhang et al. 2001; Sterling et al. 2007). In the slow-rise phase, the erupting structures rise with an approximately linear behavior. The acceleration is extremely small or not even measurable for nine of our 12 events, small for two events (H3 and H5), and moderate ($\sim 160 \pm 70 \text{ m s}^{-2}$) only for H1. The main-acceleration phase starts with a rapidly and nonlinearly increasing acceleration, indicating instability. Through experimenting with linear, quadratic, exponential, and power-law functions, we find that the ones consisting of a nonlinearly accelerating component superimposed with a linear component fit the height–time profiles best for all events. From the superiority of the superposed fit functions, as well as from the shapes of the acceleration–time profiles, we conclude, opposite to Kahler et al. (1988), that the main-acceleration phase is qualitatively different from the slow-rise phase, strongly suggesting that different physical mechanisms govern them. This implies that “runaway reconnection”, conjectured in the original tether-cutting model (Moore et al. 2001), cannot be a uniform mechanism for both phases. However, this model remains a possible model for the slow-rise phase, as suggested by many recent investigations, including the present work.

The nonlinear rise is approximately exponential for three of our six hot channel eruptions and for all six filament eruptions, while a power law describes the rise best for the remaining three hot channel eruptions. This is consistent with the result of Vršnak (2001), in which an exponential-like or power-law-like growth of the CME height is also found for a large sample of events, even valid in the higher corona. By contrast, Schrijver et al. (2008), considering two eruptions from active regions, concluded that the power-law function can yield a slightly better fit than the exponential in the main-acceleration phase. From our fit results and from the relevance of the torus instability (Section 4.3), we conjecture that the nonlinear rise is mostly exponential for the majority of eruptions. Considering the different conclusion in Schrijver et al. (2008), there appear to exist three possible reasons for the superiority of a power-law fit. First, the rise can indeed be closer to a power law when an instability is triggered by a sizeable perturbation (e.g., a sympathetic eruption or rapid flux emergence), as demonstrated in Schrijver et al. (2008). However, such a scenario does not appear to be very frequent; rather, the photospheric evolution toward an eruption is usually gradual, and sympathetic events are rare. Second, the fit functions employed in Schrijver et al. (2008) gave an advantage to the power law, which contained one more free parameter than the exponential, thus allowing for a higher flexibility. Third, and probably most importantly, a power law should be preferred if the fitting includes some data points beyond the linear phase of an instability into the saturation phase (characterized by a decreasing acceleration), as done in Schrijver et al. (2008). Since the exponential rises faster than the power law in the long run, it should yield a stronger deviation from the data points in the saturation phase. The number of data points in the main-acceleration phase is limited by its duration relative to the cadence of the observation. Not surprisingly, the quiescent filament eruptions, which provide many data points before the saturation sets in, all favor the exponential fit. Further investigation of the kinematics of eruptions from active regions is required to clearly elucidate the relevance of exponential versus power-law behavior.

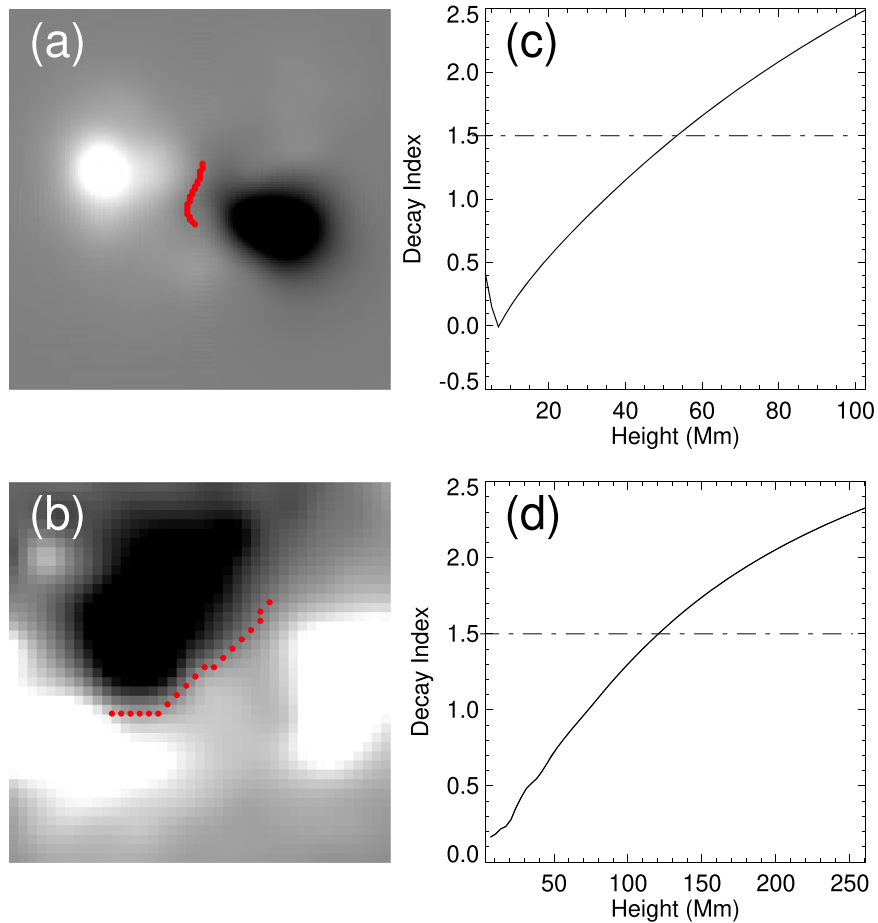


Figure 11. (a), (b) Distribution of vertical magnetic field (B_z) in the H3 and F1 source regions at the height of $1.1 R_\odot$. The red dotted lines show the section of the PIL included in averaging the decay index height profile, shown in panels (c) and (d). The theoretical value of 1.5 for the critical decay index of a toroidal flux rope is indicated by the dashed-dotted lines.

5.2. CME-flare Timing Relationship

We also study the timing relation of the evolution of CMEs to that of the associated flares. With only one exception (H4), the velocity in the main part of the CME main-acceleration phase is synchronized with the SXR and EUV light curve in the main part of the flare impulsive-rise phase in our sample. The synchronization is rather close for the majority of the events (H2, H3, H5, H6, F1, F4–F6), even very close for some of these, and moderate for the others (H1, F2, F3). In the H4 event, the hot channel evolves with a much larger volume than the flare, so the synchronization is poor, but a flare associated in time with the hot channel eruption exists as well. The timing of the peak CME acceleration relative to the peak flare energy release rate can serve as a quantitative measure of the synchronization between CME acceleration and flare energy release (Maričić et al. 2007). However, for many of our events, we cannot reliably determine the point of peak acceleration, because the hot channels tend to fade, and the quiescent filaments tend to approach the edge of the AIA field of view, before the peak acceleration is reached.

A synchronization, albeit less close, also exists in the slow-rise phase of the hot channel eruptions (again, except for H4), which then already show weak flare signatures. The integrated AIA 304 \AA emission of the source region, taken as a proxy for a flare signature in the slow-rise phase of our quiescent filament eruptions, shows a synchronization with the slow-rise velocity

in half of the events. The opposite trend is noticed in the other half; here, the enhanced absorption by the spreading of the filament masks any synchronization that might exist.

The onset times of the CME main acceleration and flare impulsive rise are found to be very close to each other for five hot channel eruptions (except the complex event H4). On the other hand, five of the six quiescent filament eruptions show a delayed onset of the impulsive flare phase. The delay is unambiguous for F4, F5, and F6, very likely for F1 and F3, and weakly indicated for F2. For F1 and F6, it is unlikely that the background level of the 304 \AA emission from the source region is so low that its flare-related rise would start as early as the time t_3 derived for the CME onset (see Figures 2(d) and 5). The delays for these five events are substantial, lying in the range of 18–103 minutes. These results are consistent with those in Maričić et al. (2007), who found a significantly delayed flare onset (by $\geq 30\%$ of the duration of the main acceleration) for six out of 18 eruptions, but mostly from active regions.

Overall, these findings agree very well with previous results that the main CME acceleration and main flare energy release, the latter being due to reconnection, are coupled (e.g., Zhang et al. 2001). They also indicate an association between the preceding slow ascent of flux and reconnection in the source region, except in those cases where a filament spreading masks any potentially related increase of the EUV flux (F1, F5, and F6). This is consistent with the conjecture that tether-cutting reconnection is an important process in this phase. In spite of

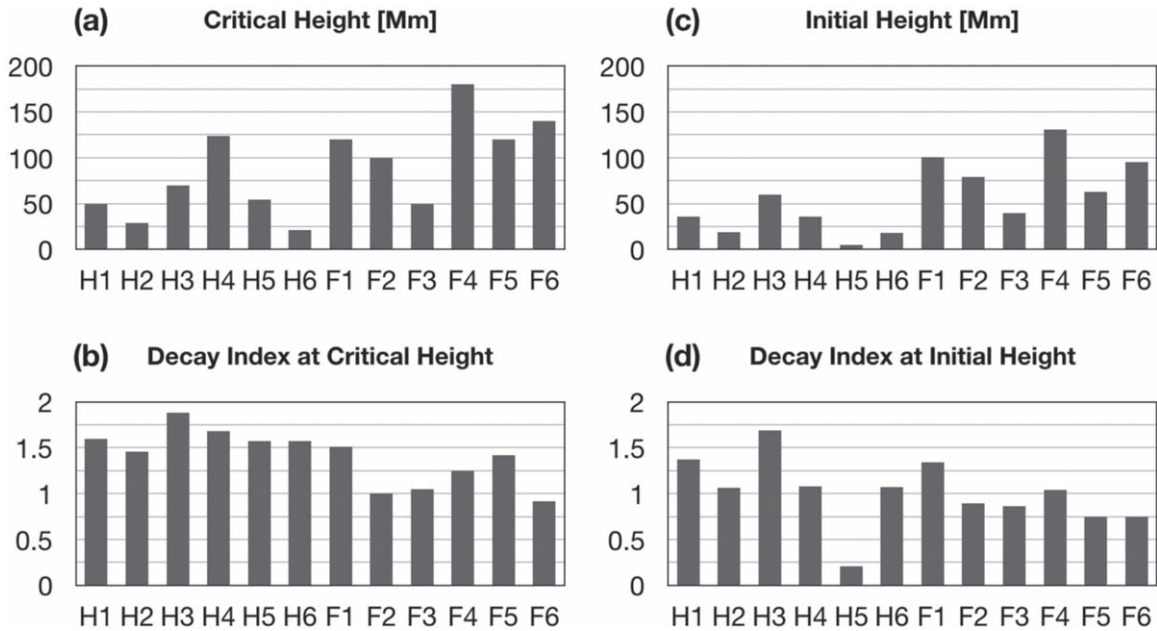


Figure 12. Distributions of the critical height h_c (a), and the corresponding decay index n_c at the onset of the main-acceleration phase (b). Panels (c) and (d) show initial height h_0 and corresponding decay index n_0 at the onset of the slow-rise phase.

these associations, the fitting also yields a clearly delayed onset of the flare impulsive phase for the majority of our quiescent filament eruptions. The latter result, although requiring substantiation from a larger sample of events, favors instability models above reconnection models for the *onset* of the main CME acceleration. This is true, in particular, if the same mechanism initiates the eruptions of quiescent filaments and from active regions, as is widely assumed.

5.3. Relevance of Torus Instability for Eruption Onset and Driving

Based on the onset time of the main acceleration, the critical height and resulting decay index are inferred. (The reliability of these values requires discussion, which we provide in Section 5.4, in comparison with other recent inferences in the literature.) For the hot channels, the decay indices are found to be close to the threshold of torus instability for the circular flux rope (1.4–1.9; Török & Kliem 2005; Kliem & Török 2006; Fan & Gibson 2007; Aulanier et al. 2010), while for the quiescent filaments, the values cluster around the threshold of torus instability for the straight flux rope (1.1–1.3; Démoulin & Aulanier 2010). This is consistent with the observations that the hot channels usually present a curved loop-like structure (e.g., Zhang et al. 2012; Cheng et al. 2013b; Li & Zhang 2013a, 2013b; Patsourakos et al. 2013; Tripathi et al. 2013; Vemareddy & Zhang 2014; Chintzoglou et al. 2015; Joshi et al. 2015; Zhou et al. 2016), whereas the quiescent filaments typically appear as a set of long and nearly straight threads, overall much closer to an only weakly bent cylinder (e.g., Yang et al. 2014; Yan et al. 2015; Li et al. 2017).

These results suggest that the torus instability of a flux rope initiates the main-acceleration phase. No association of eruption onset with the critical decay index of the torus instability is expected if magnetic reconnection is the initiating process. The onset of ideal MHD instability also naturally leads to an exponential growth of the eruptions and to the development of a feedback between the instability and reconnection during the main-acceleration phase. Once the

instability sets in, the flux rope is driven to erupt outward rapidly. With a short time delay, the fast flare reconnection, taking place in a narrow, long stretching current sheet formed below the erupting flux rope (Lin et al. 2005; Savage et al. 2010; Liu et al. 2013; Ling et al. 2014; Sun et al. 2015; Cheng et al. 2018), is switched on or strongly amplified from preceding slow tether-cutting reconnection. This produces two relevant effects: an enhancement of the force imbalance due to the transfer of the overlying flux into poloidal flux of the flux rope and the upward slingshot effect of the reconnected flux. Both of them provide an upward force that can additionally accelerate the erupting CME, which, in turn, further facilitates the development of the torus instability. That is to say, the main-acceleration phase is *expected* to be a process consisting of a combination of ideal torus instability and magnetic reconnection in a positive, mutually amplifying feedback.

Unfortunately, at present, it is still extremely difficult to figure out which mechanism (torus instability or magnetic reconnection) provides a dominant contribution in the main-acceleration phase. This might even vary from event to event. The hot channels tend to lose their equilibrium at relatively low heights. Fast reconnection then tends to commence promptly. As the involved field is strong, the two reconnection-induced effects should be very efficient, especially if the reconnection sets in almost simultaneously in a relatively elongated area below the rising flux rope. In such cases, the sudden transfer of the overlying flux to poloidal flux of the rope immediately amplifies the acceleration strongly. Similarly, the sudden upward snapping of the reconnected field lines may also efficiently contribute to the acceleration of the eruption.

For the quiescent filament eruptions, very weak flares are typically associated, manifesting as ribbons and post-flare arcades only in the 304 and 171 Å passbands. This is also common for polar crown prominence eruptions (Song et al. 2013; Gopalswamy et al. 2015). The corresponding CMEs tend to be slower, because they originate in larger source regions with weaker magnetic fields. The main acceleration starting

earlier than the flare onset suggests that the acceleration process may be first dominated by the torus instability, as the reconnection and its induced two effects should not be very efficient (weak fields and relatively large heights at which reconnection occurs). The slingshot effect, for example, turns in such cases into a weak reconnection outflow, which may deform the flux rope a little bit if it catches up to the erupting rope, but may not accelerate it considerably. Similarly, the force imbalance due to flux transfer should also not be very strong. The distance between the flux rope and the reconnecting X-line is larger, and the reconnection jet velocity is smaller compared to eruptions from active regions. Therefore, if the flare reconnection is a consequence of the ideal MHD instability, then one can expect that any delay of the flare onset, as well as the time needed to fully establish the feedback between ideal instability and reconnection, tends to be longer for erupting quiescent filaments, as found in the events studied here. The same trend is also indicated, albeit weakly, within our group of quiescent filament eruptions: the eruptions F4–F6 show the longest delay, and two of them (F4 and F6) are the slowest eruptions in the sample when only the AIA field of view is considered (see Figure 5, second column). Since any delay of reconnection onset can also depend on the magnetic topology of the source region, a close correlation with the velocity of the eruption is not expected.

For the slow-rise phase, the torus instability is unlikely to be the universal onset and driving process because the decay index at the inferred onset height is clearly subcritical for the majority of the investigated events. We argue that the slow rise of all 12 events is closely associated with slow tether-cutting magnetic reconnection. First, this is indicated by the synchronization of the velocity–time profiles and flare light curves, which is seen whenever enhanced absorption by a filament is not dominant in the light curve. Second, small-scale EUV brightenings are seen in the source regions of all events. This supports the occurrence of reconnection in the slow-rise phase but with a much slower magnetic dissipation rate than that in the main-acceleration phase. Such a slow reconnection is very critical to creating more poloidal flux and lifting the hot channels gently. This is also inferred by recent work by Liu et al. (2018), in which a hyperbolic flux tube (HFT) was identified underneath the hot channels prior to their eruption. The tether-cutting type reconnection in the HFT then proceeds slowly, due to the slow driving from the photosphere, as long as no fast driving from an MHD instability in the corona occurs, simultaneously leading to the slow rise and heating of the hot channels. The slow rise of the quiescent filaments can additionally be driven by mass draining (see Jenkins et al. 2019 and references therein). Such a feature is observed in the slow-rise phase of F2 but not in the other filament events studied here.

5.4. Estimate of Decay Index

Finally, we discuss the reliability of our estimates of the onset heights, h_c , and critical decay index values, n_c . It is clear that an accurate estimate of the onset height is as important as an accurate coronal field model for obtaining a reliable decay index. However, as pointed out in Section 4.3, with current instrumentation, a compromise between the reliability of the height–time and magnetogram data must be chosen, especially for hot channels and other rapidly evolving (fast) eruptions. For events near the limb, the $h(t)$ data from SDO/AIA have a high accuracy and cadence, yielding the most reliable onset heights,

but the magnetic data have a temporal offset of 3–4 days. For events near the disk center, the magnetic data are optimized, but STEREO/EUVI does not provide $h(t)$ data for hot channels and yields lower cadence for filaments. At present, it is not clear whether one of these choices or a compromise in the middle yields the most reliable n_c values. The former choice may be best for events from slowly evolving source regions, and the latter choice may be best for very slowly rising eruptions.

Our sample of quiescent filaments erupting from longitudes $\leq 60^\circ$ (Table 1) represents a good compromise for this category of events. This choice yields accurate and reliable onset heights from the combination of AIA and EUVI data and mostly very reliable and nearly up-to-date magnetograms of the source region. On the other hand, the temporal offset of the magnetogram data for the five hot channel eruptions near the limb introduces an uncertainty of the computed coronal field and inferred decay index values. We argue, however, that substantial errors in the decay index values are unlikely, because the decay index at the relevant onset heights is primarily determined by the large-scale structure of the active-region magnetograms. The typical height for torus instability onset is about the half-distance, L_f , between the main photospheric flux concentrations that provide the background field (this is where $n = 1.5$ in a bipole). At this height, the large-scale structure of the photospheric field at scales $\sim L_f$ determines the structure of the coronal background field and its decay index. Typically, the large-scale structure changes only slowly for active regions after their emergence phase, i.e., at most moderately in the given time span. Figure 10, discussed in Section 4.3, confirms that the large-scale structure does not show strong changes during the relevant period for any of our hot channel events from the limb. The flux cancellation seen in the evolution toward the eruptions H2, H3, and H6 at a scale $\ll L_f$ will influence $n(h)$ primarily at scales $h \ll L_f$ and only weakly at $h \sim h_c$. Although the measured field strengths become less reliable closer to the limb, the geometric evolution can still be judged, especially the evolution of L_f . The effect of magnetogram evolution on the decay index values in the relevant height range ($h \sim L_f$) can be quantitatively studied using a sample of eruptions from active regions near the central meridian. This will be done in a follow-up study, to support the methodology chosen here.

To illustrate the complexity of the methodological approach to the problem, including the very important role of precise $h(t)$ data, it is instructive to compare our values with those published very recently by Vasantharaju et al. (2019, henceforth V19), Zou et al. (2019, henceforth Z19), and Myshyakov & Tsvetkov (2020). V19 and Z19 determined the onset of the main-acceleration phase of erupting filaments/prominences using the same fit function $h_2(t)$ with $t_0 = 0$ and the same expression for the onset time (our t_3), and they also inferred the critical decay index at the obtained onset height. V19 selected seven filament eruptions from active regions and three from between active regions, so-called intermediate filament eruptions. There is a salient difference in the results for the critical decay index, found to lie in the range 0.8–1.2, averaging to ~ 1.0 , for the active-region filaments (0.8–1.3 if the intermediate filaments are included) in V19, while our critical decay indices for the eruptions from active regions fall in the range 1.5–1.9, with an average of 1.6. On the other hand, Z19 found the critical decay index for filament

eruptions from active regions to lie in the range 0.4–2.5, which is consistent with our range (although far broader), with an average of ~ 1.5 , close to our average.

The analysis of the kinematic evolution in V19 and Z19 is very similar to ours, with probably less-precise height data than that in V19 and Z19 because their source regions were chosen mostly on disk (in a range of intermediate longitudes $\pm 40^\circ$ – 80° in V19 and without any longitude selection in Z19). This is a likely reason for the large scatter of the n_c values in Z19 but can hardly explain the strong systematic difference to V19. The main reason causing the latter, we speculate, is that V19 underestimated the critical height. They found the critical heights for their seven eruptions from active regions to lie in the range $h_c = 10$ – 38 Mm, with an average of 22 Mm. This is much smaller than our $h_c = 21$ – 124 Mm, with an average of 57 Mm. The main reason appears to be the fact that they included a much earlier part of the slow rise in their analysis of the kinematics, possibly due to the low cadence available from STEREO. The early part typically presents a very small velocity (< 1 km s $^{-1}$; Xing et al. 2018). Such a small velocity results in the crossing of the linear and exponential components in $h_2(t)$, i.e., the onset time, shifting toward an earlier time, thus giving rise to a smaller onset height. Additional reasons could be that (1) filament heights, as used by V19, may fall systematically below the heights of flux ropes (hot channels used here), as suggested by Zuccarello et al. (2016), especially during the main-acceleration phase, (2) several of the events in V19 actually originated in areas of a rather dispersed field, (3) most of their events originated from longitudes $> 50^\circ$, where the daily update of the synoptic magnetogram has only a limited or no effect, (4) the different choice of coronal field model has a systematic effect on the decay index estimates, (5) power-law fits may tend to yield larger onset heights, as is the case for our events H5 and H6, and (6) the samples of active-region events still have a relatively small size.

Specifically, V19 computed the potential field in the PFSS approximation, while we use the Green function in a Cartesian box. The latter assumes that all sources of the coronal field are localized under the magnetogram area, so that the field asymptotically decreases like a dipole field, i.e., $n \rightarrow 3$ for $h \rightarrow \infty$. The PFSS approximation implies the presence of the heliospheric current sheet outside the source surface. This additional source changes the asymptotic behavior of the field to a significantly slower decrease, $n < 3$. From our experience with applying the PFSS method to > 50 cases, the decay index in the height range approaching the source surface scatters strongly, with values around 2.2 being most common. Irrespective of this specific value, it is clear that the PFSS model tends to drop the decay index to values lower than the ones in the corresponding potential field computed with the Green function. This is consistent also (1) with the slightly smaller average critical decay index in Z19 compared to ours and (2) with the high critical decay index values of 1.5–1.8 for three quiescent filament eruptions found by Myshyakov & Tsvetkov (2020), who used the Green function to compute the coronal field. The critical values n_c inferred in the literature for eruptions from the quiet Sun are typically smaller than those for eruptions from active regions, similar to our results in Section 4.3. While this is plausible from the geometrical difference (typically flatter versus typically more arched erupting structures, respectively), an influence of the universal use of the PFSS model for eruptions from the quiet Sun, except

in the study by Myshyakov & Tsvetkov (2020), cannot be excluded.

From the above discussion, it is clear that a reliable determination of the decay index at the onset of eruptions requires precise height–time measurements at high cadence, a reliable magnetogram, and an appropriate choice of extrapolation method. All of the factors listed above, which definitely or potentially influence the inferred decay index values, will be addressed in subsequent investigations.

6. Conclusions

We obtain the following conclusions, valid in the whole range of rise velocities reached by the 12 studied eruptions.

1. The fitting confirms that the slow-rise and main-acceleration phases of solar eruptions are qualitatively different, indicating different dominant mechanisms.
2. The slow-rise phase is well approximated by a linear or quadratic ascent, with the majority of events showing a very small acceleration. An obvious quadratic contribution is found only in three of our six hot channel events.
3. The main-acceleration phase is characterized by an exponential rise in the majority of events, indicating instability. For a small fraction of the events (three in our sample), the rise is closer to a power law. Further studies of data with higher cadence are required to clarify the relevance of power-law behavior in this phase.
4. The kinematic evolution of the eruptions tends to be synchronized with reconnection in the source volume as represented by the SXR or EUV light curve of the associated flare. The synchronization is found in both the slow-rise and main-acceleration phases and is often but not always close. This indicates a strong role for slow tether-cutting reconnection in the slow-rise phase and a positive feedback between ideal MHD instability and fast flare reconnection in the main-acceleration phase.
5. The onset times of CME main acceleration and flare impulsive rise lie close to each other for the hot channel eruptions, except for one complex event (H4). The delays scatter within 3 minutes, less than their estimated uncertainty. On the other hand, a delayed onset of the impulsive flare phase is found in the majority of our quiescent filament eruptions (five out of six) and weakly indicated in the remaining one. This delay and its trend to be bigger for slower eruptions are consistent with the conjecture that an ideal MHD instability initiates and initially drives solar eruptions.
6. The decay index of the ambient field at the starting height of the main-acceleration phase lies close to the threshold of the torus instability for all 12 events (1.6 ± 0.1 on average for the typically arched hot channel eruptions from active regions and 1.2 ± 0.2 on average for the much flatter erupting quiescent filaments). This suggests that the torus instability initiates and initially drives the main-acceleration phase in the majority of solar eruptions. However, the accuracy of the decay-index calculation is limited by the lack of reliable magnetograms for five of our hot channel events that occur close to or above the limb. We believe that this limitation does not change our main conclusion, but further studies need to be pursued to confirm it.

Code availability: The codes used for measuring and fitting height–time data are available at the website <http://spaceweather.gmu.edu/public/xcheng/fit/>.

We thank the ISSI team on “Decoding the Pre-Eruptive Magnetic Configuration of Coronal Mass Ejections”, led by S. Patsourakos & A. Vourlidas, for stimulating the research presented here. We also acknowledge constructive comments by the referee, which helped improving the clarity of the manuscript. SDO is a mission of NASA’s Living With a Star Program. STEREO/SECCHI data are provided by a consortium of NRL (US), LMSAL (US), NASA/GSFC (US), RAL (UK), UBHAM (UK), MPS (Germany), CSL (Belgium), IOTA (France), and IAS (France). X.C., C.X., Z.J.Z., and M.D. D. are supported by NSFC grants 11722325, 11733003, 11790303, 11790300, Jiangsu NSF grant BK20170011, the “Dengfeng B” program of Nanjing University, and the Alexander von Humboldt foundation. B.K. acknowledges support by the DFG and NSFC through the collaborative grant KL 817/8-1/NSFC and support by NASA through grants NNX16AH87G, 80NSSC17K0016, 80NSSC19K0082, and 80NSSC19K0860. T.T. was supported by NASA’s HSR program (award No. 80NSSCK0858), NSF’s Solar Terrestrial program (award No. AGS-1923377), and NSF’s PREEVENTS program (award No. ICER-1854790). J.Z. is supported by NASA grant NNH17ZDA001N-HSWO2R.

ORCID iDs

X. Cheng  <https://orcid.org/0000-0003-2837-7136>
 B. Kliem  <https://orcid.org/0000-0002-5740-8803>
 T. Török  <https://orcid.org/0000-0003-3843-3242>
 M. D. Ding  <https://orcid.org/0000-0002-4978-4972>

References

- Alexander, D., Metcalf, T. R., & Nitta, N. V. 2002, *GeoRL*, **29**, 1403c
 Antiochos, S. K., DeVore, C. R., & Klimchuk, J. A. 1999, *ApJ*, **510**, 485
 Aulanier, G., Török, T., Démoulin, P., & DeLuca, E. E. 2010, *ApJ*, **708**, 314
 Baty, H. 2001, *A&A*, **367**, 321
 Bein, B. M., Berkebile-Stoiser, S., Veronig, A. M., Temmer, M., & Vršnak, B. 2012, *ApJ*, **755**, 44
 Brueckner, G. E., Howard, R. A., Koomen, M. J., Korendyke, C. M., et al. 1995, *SoPh*, **162**, 357
 Chen, H., Zhang, J., Cheng, X., et al. 2014, *ApJL*, **797**, L15
 Cheng, X., Ding, M. D., Guo, Y., et al. 2014a, *ApJ*, **780**, 28
 Cheng, X., Ding, M. D., & Zhang, J. 2010, *ApJ*, **712**, 1302
 Cheng, X., Ding, M. D., Zhang, J., et al. 2014b, *ApJL*, **789**, L35
 Cheng, X., Li, Y., Wan, L. F., et al. 2018, arXiv:1808.06071
 Cheng, X., Zhang, J., Ding, M. D., et al. 2013a, *ApJL*, **769**, L25
 Cheng, X., Zhang, J., Ding, M. D., Liu, Y., & Poomvises, W. 2013b, *ApJ*, **763**, 43
 Cheng, X., Zhang, J., Liu, Y., & Ding, M. D. 2011, *ApJL*, **732**, L25
 Cheng, X., Zhang, J., Saar, S. H., & Ding, M. D. 2012, *ApJ*, **761**, 62
 Chintzoglou, G., Patsourakos, S., & Vourlidas, A. 2015, *ApJ*, **809**, 34
 Démoulin, P., & Aulanier, G. 2010, *ApJ*, **718**, 1388
 Dere, K. P., Brueckner, G. E., Howard, R. A., Michels, D. J., & Delaboudiniere, J. P. 1999, *ApJ*, **516**, 465
 Fan, Y., & Gibson, S. E. 2003, *ApJL*, **589**, L105
 Fan, Y., & Gibson, S. E. 2004, *ApJ*, **609**, 1123
 Fan, Y., & Gibson, S. E. 2007, *ApJ*, **668**, 1232
 Forbes, T. G. 2000, *JGR*, **105**, 23153
 Forbes, T. G., & Isenberg, P. A. 1991, *ApJ*, **373**, 294
 Gallagher, P. T., Lawrence, G. R., & Dennis, B. R. 2003, *ApJL*, **588**, L53
 Gary, G. A., & Moore, R. L. 2004, *ApJ*, **611**, 545
 Gibson, S. E., & Fan, Y. 2006, *JGRA*, **111**, 12103
 Gilbert, H. R., Holzer, T. E., Burkepile, J. T., & Hundhausen, A. J. 2000, *ApJ*, **537**, 503
 Gopalswamy, N., Shimojo, M., Lu, W., et al. 2003, *ApJ*, **586**, 562
 Gopalswamy, N., Yashiro, S., & Akiyama, S. 2015, *ApJ*, **809**, 106
 Gosling, J. T. 1993, *JGR*, **98**, 18937
 Green, L. M., Török, T., Vršnak, B., Manchester, W., & Veronig, A. 2018, *SSRv*, **214**, 46
 Guo, Y., Schmieder, B., Démoulin, P., et al. 2010, *ApJ*, **714**, 343
 Hassani, A., & Kliem, B. 2016, *ApJ*, **832**, 106
 Howard, R. A., Moses, J. D., Vourlidas, A., et al. 2008, *SSRv*, **136**, 67
 Illing, R. M. E., & Hundhausen, A. J. 1983, *JGR*, **88**, 10210
 Inoue, S., Hayashi, K., Shiota, D., Magara, T., & Choe, G. S. 2013, *ApJ*, **770**, 79
 Jenkins, J. M., Hopwood, M., Démoulin, P., et al. 2019, *ApJ*, **873**, 49
 Ji, H., Wang, H., Schmahl, E. J., Moon, Y.-J., & Jiang, Y. 2003, *ApJL*, **595**, L135
 Jiang, C., Wu, S. T., Feng, X., & Hu, Q. 2014, *ApJL*, **786**, L16
 Joshi, N. C., Liu, C., Sun, X., et al. 2015, *ApJ*, **812**, 50
 Kahler, S. W., Moore, R. L., Kane, S. R., & Zirin, H. 1988, *ApJ*, **328**, 824
 Karpen, J. T., Antiochos, S. K., & DeVore, C. R. 2012, *ApJ*, **760**, 81
 Kliem, B., Lin, J., Forbes, T. G., Priest, E. R., & Török, T. 2014, *ApJ*, **789**, 46
 Kliem, B., Titov, V. S., & Török, T. 2004, *A&A*, **413**, L23
 Kliem, B., & Török, T. 2006, *PhRvL*, **96**, 255002
 Kwon, R.-Y., Zhang, J., & Olmedo, O. 2014, *ApJ*, **794**, 148
 Lemen, J. R., Title, A. M., Akin, D. J., et al. 2012, *SoPh*, **275**, 17
 Li, L. P., & Zhang, J. 2013a, *A&A*, **552**, L11
 Li, Q., Deng, N., Jing, J., & Wang, H. 2017, *ApJ*, **841**, 112
 Li, T., & Zhang, J. 2013b, *ApJL*, **778**, L29
 Li, T., Zhang, J., & Ji, H. 2015, *SoPh*, **290**, 1687
 Lin, J., Ko, Y.-K., Sui, L., et al. 2005, *ApJ*, **622**, 1251
 Lin, J., & van Ballegoijen, A. A. 2002, *ApJ*, **576**, 485
 Ling, A. G., Webb, D. F., Burkepile, J. T., & Cliver, E. W. 2014, *ApJ*, **784**, 91
 Liu, R., Liu, C., Wang, S., Deng, N., & Wang, H. 2010, *ApJL*, **725**, L84
 Liu, T., Su, Y., Cheng, X., van Ballegoijen, A., & Ji, H. 2018, *ApJ*, **868**, 59
 Liu, W., Chen, Q., & Petrosian, V. 2013, *ApJ*, **767**, 168
 Mackay, D. H., Karpen, J. T., Ballester, J. L., Schmieder, B., & Aulanier, G. 2010, *SSRv*, **151**, 333
 Maričić, D., Vršnak, B., Stanger, A. L., et al. 2007, *SoPh*, **241**, 99
 Markwardt, C. B. 2009, in ASP Conf. Ser. 411, *Astronomical Data Analysis Software and Systems XVIII*, ed. D. A. Bohlender, D. Durand, & P. Dowler (San Francisco, CA: ASP), 251
 McCauley, P. I., Su, Y. N., Schanche, N., et al. 2015, *SoPh*, **290**, 1703
 Moore, R. L., Sterling, A. C., Hudson, H. S., & Lemen, J. R. 2001, *ApJ*, **552**, 833
 Munro, R. H., Gosling, J. T., Hildner, E., et al. 1979, *SoPh*, **61**, 201
 Myshyakov, I., & Tsvetkov, T. 2020, *ApJ*, **889**, 28
 Neupert, W. M., Thompson, B. J., Gurman, J. B., & Plunkett, S. P. 2001, *JGR*, **106**, 25215
 Nindos, A., Patsourakos, S., Vourlidas, A., & Tagikas, C. 2015, *ApJ*, **808**, 117
 Olmedo, O., & Zhang, J. 2010, *ApJ*, **718**, 433
 Ouyang, Y., Yang, K., & Chen, P. F. 2015, *ApJ*, **815**, 72
 Palacios, J., Cid, C., Guerrero, A., Saiz, E., & Cerrato, Y. 2015, *A&A*, **583**, A47
 Patsourakos, S., Vourlidas, A., & Kliem, B. 2010a, *A&A*, **522**, A100
 Patsourakos, S., Vourlidas, A., & Stenborg, G. 2010b, *ApJL*, **724**, L188
 Patsourakos, S., Vourlidas, A., & Stenborg, G. 2013, *ApJ*, **764**, 125
 Pesnell, W. D., Thompson, B. J., & Chamberlin, P. C. 2012, *SoPh*, **275**, 3
 Qiu, J., Wang, H., Cheng, C. Z., & Gary, D. E. 2004, *ApJ*, **604**, 900
 Riley, P., Lionello, R., Mikić, Z., & Linker, J. 2008, *ApJ*, **672**, 1221
 Sakurai, T. 1976, *PASJ*, **28**, 177
 Savage, S. L., McKenzie, D. E., Reeves, K. K., Forbes, T. G., & Longcope, D. W. 2010, *ApJ*, **722**, 329
 Schatten, K. H., Wilcox, J. M., & Ness, N. F. 1969, *SoPh*, **6**, 442
 Schou, J., Scherrer, P. H., Bush, R. I., et al. 2012, *SoPh*, **275**, 229
 Schrijver, C. J., Elmore, C., Kliem, B., Török, T., & Title, A. M. 2008, *ApJ*, **674**, 586
 Seaton, D. B., Bartz, A. E., & Darnel, J. M. 2017, *ApJ*, **835**, 139
 Sheeley, N. R., Jr., Warren, H. P., & Wang, Y. M. 2007, *ApJ*, **671**, 926
 Shen, Y., Liu, Y., & Su, J. 2012, *ApJ*, **750**, 12
 Sinha, S., Srivastava, N., & Nandy, D. 2019, *ApJ*, **880**, 84
 Song, H. Q., Chen, Y., Ye, D. D., et al. 2013, *ApJ*, **773**, 129
 Song, H. Q., Cheng, X., Chen, Y., et al. 2017, *ApJ*, **848**, 21
 Song, H. Q., Zhou, Z. J., Li, L. P., et al. 2018, *ApJL*, **864**, L37
 Sterling, A. C., Harra, L. K., & Moore, R. L. 2007, *ApJ*, **669**, 1359
 Sterling, A. C., Moore, R. L., & Freeland, S. L. 2011, *ApJL*, **731**, L3
 Su, Y., van Ballegoijen, A., McCauley, P., et al. 2015, *ApJ*, **807**, 144
 Sun, J. Q., Cheng, X., Ding, M. D., et al. 2015, *NatCo*, **6**, 7598
 Sun, X. 2018, arXiv:1801.04265

- Temmer, M., Veronig, A. M., Kontar, E. P., Krucker, S., & Vršnak, B. 2010, *ApJ*, 712, 1410
- Temmer, M., Veronig, A. M., Vršnak, B., et al. 2008, *ApJL*, 673, L95
- Török, T., Berger, M. A., & Kliem, B. 2010, *A&A*, 516, A49
- Török, T., & Kliem, B. 2005, *ApJL*, 630, L97
- Török, T., Kliem, B., & Titov, V. S. 2004, *A&A*, 413, L27
- Tripathi, D., Reeves, K. K., Gibson, S. E., Srivastava, A., & Joshi, N. C. 2013, *ApJ*, 778, 142
- Vasantharaju, N., Vemareddy, P., Ravindra, B., & Doddamani, V. H. 2019, *ApJ*, 885, 89
- Vemareddy, P., & Zhang, J. 2014, *ApJ*, 797, 80
- Veronig, A. M., Podladchikova, T., Dissauer, K., et al. 2018, *ApJ*, 868, 107
- Vourlidas, A., Wu, S. T., Wang, A. H., Subramanian, P., & Howard, R. A. 2003, *ApJ*, 598, 1392
- Vršnak, B. 2001, *JGR*, 106, 25249
- Wan, L., Cheng, X., Shi, T., Su, W., & Ding, M. D. 2016, *ApJ*, 826, 174
- Webb, D. F., Forbes, T. G., Aurass, H., et al. 1994, *SoPh*, 153, 73
- Webb, D. F., & Hundhausen, A. J. 1987, *SoPh*, 108, 383
- Williams, D. R., Török, T., Démoulin, P., van Driel-Gesztelyi, L., & Kliem, B. 2005, *ApJL*, 628, L163
- Wood, B. E., Howard, R. A., & Linton, M. G. 2016, *ApJ*, 816, 67
- Xing, C., Li, H. C., Jiang, B., Cheng, X., & Ding, M. D. 2018, *ApJ*, 857, L14
- Yan, X.-L., Xue, Z.-K., Xiang, Y.-Y., & Yang, L.-H. 2015, *RAA*, 15, 1725
- Yang, S., Zhang, J., Liu, Z., & Xiang, Y. 2014, *ApJL*, 784, L36
- Yashiro, S., Akiyama, S., Gopalswamy, N., & Howard, R. A. 2006, *ApJL*, 650, L143
- Zhang, J., Cheng, X., & Ding, M.-D. 2012, *NatCo*, 3, 747
- Zhang, J., & Dere, K. P. 2006, *ApJ*, 649, 1100
- Zhang, J., Dere, K. P., Howard, R. A., Kundu, M. R., & White, S. M. 2001, *ApJ*, 559, 452
- Zhang, J., Dere, K. P., Howard, R. A., & Vourlidas, A. 2004, *ApJ*, 604, 420
- Zhou, G. P., Zhang, J., & Wang, J. X. 2016, *ApJL*, 823, L19
- Zou, P., Jiang, C., Wei, F., Zuo, P., & Wang, Y. 2019, *ApJ*, 884, 157
- Zuccarello, F. P., Aulanier, G., & Gilchrist, S. A. 2016, *ApJL*, 821, L23